The Astrophysical Journal, 760:149 (25pp), 2012 December 1 doi:10.1088/0004-637X/760/2/149

SPITZER AND *HERSCHEL* MULTIWAVELENGTH CHARACTERIZATION OF THE DUST CONTENT OF EVOLVED H II REGIONS

R. Paladini[1], G. Umana[2], M. Veneziani[3], A. Noriega-Crespo[3], L. D. Anderson[4], F. Piacentini[5], D. Pinheiro Gonçalves[6], D. Paradis[7], C. T. Tibbs[8], J.-P. Bernard[7], and P. Natoli[9]
[1] NASA Herschel Science Center, California Institute of Technology, 1200, East California Boulevard, Pasadena, CA 91125, USA; paladini@ipac.caltech.edu
[2] INAF-Osservatorio Astrofisico di Catania, Via S. Sofia 78, I-95123 Catania, Italy
[3] Infrared Processing and Analysis Center, California Institute of Technology, 1200, East California Boulevard, Pasadena, CA 91125, USA
[4] Department of Physics, West Virginia University, Morgantown, WV 26506, USA
[5] Dipartimento di Fisica, Universita' di Roma La Sapienza, I-00185 Roma, Italy
[6] Department of Astronomy and Astrophysics, University of Toronto 50 George Street, Toronto, ON M5S 3H4, Canada
[7] Centre d'Etude Spatiale des Rayonnements, 9 Avenue du Colonel Roche, F-31028 Toulouse Cedex 4, France
[8] Spitzer Science Center, California Institute of Technology, 1200, East California Boulevard, Pasadena, CA 91125, USA
[9] Istituto Nazionale di Fisica Nucleare, Sezione Ferrara, I-44100 Ferrara, Italy
Received 2012 February 12; accepted 2012 October 11; published 2012 November 16

ABSTRACT

We have analyzed a uniform sample of 16 evolved H II regions located in a $2^\circ \times 2^\circ$ Galactic field centered at $(l,b) = (30^\circ, 0^\circ)$ and observed as part of the *Herschel* Hi-GAL survey. The evolutionary stage of these H II regions was established using ancillary radio-continuum data. By combining Hi-GAL PACS (70 μm, 160 μm) and SPIRE (250 μm, 350 μm, and 500 μm) measurements with MIPSGAL 24 μm data, we built spectral energy distributions of the sources and showed that a two-component gray-body model is a good representation of the data. In particular, wavelengths >70 μm appear to trace a cold dust component, for which we estimated an equilibrium temperature of the big grains (BGs) in the range 20–30 K, while for $\lambda < 70$ μm, the data indicate the presence of a warm dust component at temperatures of the order of 50–90 K. This analysis also revealed that dust is present in the interior of H II regions, although likely not in a large amount. In addition, the data seem to corroborate the hypothesis that the main mechanism responsible for the (partial) depletion of dust in H II regions is radiation-pressure-driven drift. In this framework, we speculated that the 24 μm emission that spatially correlates with ionized gas might be associated with either very small grain or BG replenishment, as recently proposed for the case of wind-blown bubbles. Finally, we found that evolved H II regions are characterized by distinctive far-IR and submillimeter colors, which can be used as diagnostics for their identification in unresolved Galactic and extragalactic regions.

Key words: dust, extinction – Galaxy: general – H II regions

Online-only material: color figures

1. INTRODUCTION

H II regions are sites of ionized gas surrounding OB associations and represent powerful laboratories for understanding the mechanisms regulating massive star formation. Their evolutionary sequence spans different phases, from the hypercompact (HCH II) phase, in which the newly formed star is still fully embedded in its dust cocoon, to the evolved one, when most of the natal material has been ejected from the birth site. Intermediate phases are represented by ultracompact (UCH II) and compact H II regions. Each of these stages is characterized by critical values of electron density, n_e, and linear diameter (Kurtz 2005): HCH II regions have extremely high electron density ($n_e > 10^6$ cm^{-3}) and small sizes (diameters <0.05 pc), UCH II and compact H II regions have lower n_e ($n_e \sim 10^3$–10^4 cm^{-3}) and larger diameters (<0.1–0.5 pc), while evolved H II regions present even lower electron densities ($n_e \sim 10^2$ cm^{-3}) and diameters of the order of several parsecs.

The emission properties also vary with evolutionary stage. The radio emission is dominated, in all cases, by free–free emission associated with ionized gas. However, HCH II, UCH II, and occasionally (depending on n_e) compact H II regions have an optically thick spectrum for frequencies from a few to several GHz. On the contrary, the radio spectrum of an evolved H II region is optically thin already at ∼1 GHz. Both young and old sources present radio recombination lines (RRLs), although HCH II are characterized by substantially broader lines, likely due to pressure broadening and gas bulk motions. All evolutionary phases, with the exception of HCH II (Kurtz 2005), are very bright at far-IR and submillimeter (sub-mm) wavelengths. This emission has often been ascribed to the presence of dust grains. However, it is not clear whether dust is directly associated with H II regions or rather with their surrounding photodissociation regions (PDRs; see Hollenbach & Tielens (1997) for a complete review), since the historical lack of resolving power in the existing IR data has long prevented us from distinguishing these two components. This elusive separation has led many studies to use large photometric apertures which often included both the actual H II region and the PDR, with the consequence that the derived properties were a global average over intrinsically widely different regions. In fact, while an H II region is by definition the region in space where the gas is fully ionized, the PDR is mainly neutral, characterized by an $A_V > 1$. In addition, the intensity of the radiation field, as density, is not the same inside or outside the H II region, as both scale with distance from the ionizing OB association.

This situation has dramatically changed with the release of high-sensitivity, high-resolution radio (MAGPIS; Helfand et al. 2006) and IR (GLIMPSE, Benjamin et al. 2003; MIPSGAL survey, Carey et al. 2009; Hi-GAL, Molinari et al. 2010) data, which allow the clear identification of an H II region from its PDR, thus offering the unprecedented possibility of carrying

out systematic investigations of the specific properties of each of these environments. An example of what is now possible is demonstrated by the work of Povich et al. (2007). These authors used GLIMPSE and *Midcourse Space Experiment* (*MSX*; Price et al. 2001) data to perform a multiwavelength study of the M17 complex, and found that the spectral energy distribution (SED) from the H II region peaks at shorter wavelengths and has a qualitatively different shape than the SED from the PDR. They also showed that different gas and dust components are mostly distributed in mutually exclusive regions: hot plasma occupies the very inner part of the H II region, warm ionized gas defines the cavity walls, warm dust permeates the ionized gas, and polycyclic aromatic hydrocarbons (PAHs) surround the whole star-forming complex, tracing the PDR.

In this paper, we make use of the newly available data to investigate the IR properties of the interior of evolved H II regions. We also address the question—from the observational point of view—of whether dust grains survive the extreme conditions (i.e., intense UV photon flux and radiation pressure, stellar winds, and high temperatures) which characterize this type of environment. Remarkably, evolved H II regions, due to their large physical size, are ideal candidates for carrying out such analysis, as they allow us to take full advantage of the high spatial resolution (e.g., from a few to tens of arcsecs) of these new data sets.

The paper is organized as follows. In Sections 2 and 3, we illustrate the database and the source selection criteria. In Section 4, we generate source SEDs and describe the modeling procedure. In Section 5, we discuss our expectations, based on observations and theoretical predictions, of finding dust associated with a warm (10^4 K) gas. In Section 6, we show the relative spatial distribution of different populations of grains inferred by our multiwavelength data set. In Section 7, we compute the IR excess for each source and discuss its implications. In Section 8, we create color–magnitude and color–color plots, and show how these can be used for the identification of unresolved H II regions with respect to other classes of sources. We provide final remarks and conclusions in Section 9.

2. THE DATA

The bulk of the data is from the *Herschel* infrared Galactic Plane Survey (Hi-GAL). Hi-GAL (Molinari et al. 2010) consists in the observations of the first and fourth Galactic quadrants using the PACS (Poglitsch et al. 2010) and SPIRE (Griffin et al. 2010) instruments. The observations were carried out in parallel mode at 70 μm and 160 μm (PACS), and at 250 μm, 350 μm, and 500 μm (SPIRE), with an angular resolution from 6″ (70 μm) to 35″ (500 μm). During the *Herschel* Science Demonstration Phase (SDP), two Hi-GAL fields were observed. The fields are centered, for $b = 0^\circ$, at $l = 30^\circ$ and $l = 59^\circ$, and extend 2° in both latitude and longitude. The data were processed with the ROMAGAL pipeline (Traficante et al. 2011), which allows for an accurate reconstruction of both compact and extended emission. Since the SDP data were taken early in the mission, corrective factors specific to extended emission were applied. In particular, PACS 70 μm and 160 μm data were divided by 1.05 and 1.29, while SPIRE 250 μm, 350 μm, and 500 μm data were multiplied, respectively, by 1.02, 1.05, and 0.94. For the calibration uncertainties, we assumed 20% for both PACS and 15% for SPIRE (Bernard et al. 2010). We complemented the far-IR and sub-mm *Herschel* observations, with MIPS 24 μm (6″) and IRAC 8 μm (2″) data obtained by the MIPS Galactic Plane Survey (MIPSGAL) and by the Galactic Legacy Infrared Mid-Plane Survey Extraordinaire (GLIMPSE) survey. We adopted a 10% calibration error at both wavelengths (S. Carey 2010, private communication). To overcome the occasional problem (e.g., the core of G39.8−0.3) posed by hard-saturated pixels in the MIPS 24 μm data, we replaced the MIPS 24 μm data with the combined MIPS 24 μm and *MSX* 21 μm images produced by the MIPSGAL team and available to the members of the consortium. These images were generated taking into account appropriate color corrections and wavelength scaling (S. Carey 2010, private communication).

We also made use of archival single-dish 6 cm data (see Section 3), which provided the basis for our source selection, and allowed us to constrain the evolutionary phase of the H II regions in the sample. In addition, we used the Multi-Array Galactic Plane Imaging Survey (MAGPIS) high-resolution 20 cm data for a more accurate determination of the boundary of the H II regions and to perform our photometric measurements (Section 4).

3. SOURCE SELECTION AND DEFINITION OF THE SAMPLE

Since the launch of *Spitzer* in 2003 August (Werner et al. 2004) and then of *Herschel* in 2009 May (Pilbratt et al. 2010), a steady flow of papers addressed multiwavelength high-resolution investigations of Galactic H II regions. Apart for a few exceptions (e.g., the aforementioned Povich et al. (2007) work on M17, or the investigation of Flagey et al. (2011) of M16), all these studies (e.g., Watson et al. 2008; Deharveng et al. 2010; Zavagno et al. 2010; etc.) targeted bubble H II regions only. These sources are typically characterized by a common IR "structure": 8 μm emission, dominated by PAH features, encloses the bubble; the bubble itself is filled with 24 μm emission, and this spatially correlates with free–free emission associated with ionized gas. In this work, one of our goals is to investigate if it is possible to extend and generalize to other classes of H II regions the results obtained from the analysis of bubbles. For this purpose, we focused our attention on H II regions spanning a variety of morphological types. In order to assure uniformity of the sample, we required, for the selected sources, the availability of ancillary data allowing us to assess their evolutionary stage.

The starting point of our selection was the catalog of Paladini et al. (2003). While for $29^\circ < l < 31^\circ$, $|b| < 1^\circ$, the catalog lists 30 H II regions, for $58^\circ < l < 60^\circ$, $|b| < 1^\circ$, we found only two sources. Therefore, we concentrated our analysis on the Hi-GAL SDP field centered at $l = 30^\circ$. Out of the 30 cataloged sources falling in the $l = 30^\circ$ field, we made a further selection, by favoring those sources for which coordinates are known at least at arcminute precision, and an estimate of the distance is available. We note that the distance information is central to our study, since it not only allows us to compute the luminosity of the sources, but also makes it possible to generate the linear longitude and latitude profiles discussed in Section 6. The final source selection consists of 16 objects, including well-studied H II regions such as N49 (G288−0.2; Churchwell et al. 2006; Everett & Churchwell 2010; Draine 2011) and W43 (G30.8−0.3; Bally et al. 2010). Table 1 gives details relative to each source, namely: source name (Column 1), Galactic coordinates (Columns 2 and 3), 6 cm flux (Column 4), Galactocentric distance (R, Column 5), heliocentric distance (D, Column 6), far-distance solution in case of distance ambiguity (D_f, Column 7), electron temperature (T_e, Column 8), emission measure derived from single-dish ($EM_{6\,cm}$, Column 9)

Table 1
Sample of Evolved H II Regions

Name (deg)	l (deg)	b (Jy)	$S_{6\,cm}$ (kpc)	R (kpc)	D (kpc)	D_f (K)	T_e (pc cm^{-6})	$EM_{6\,cm}$ (pc cm^{-6})	$EM_{20\,cm}$ (pc cm^{-6})	EM_{shell} (cm^{-3})	$n_{e,6\,cm}$ (cm^{-3})	$n_{e,20\,cm}$ (cm^{-3})	$n_{e,shell}$
G28.8−0.2	28.823	−0.226	1.47	4.5	5.5	...	5934	8.2e4	4.4e4	...	152.7	95.9	...
G29.0−0.6	28.983	−0.603	1.01	5.8	3.4	...	6417	5.3e4	2.6e4	7.0e6	152.7	91.3	5.9e3
G29.1−0.0	29.136	−0.042	1.85	5.8	11.5	...	6417	2.7e4	7.4e4	...	43.9	91.7	...
G29.1+0.4	29.139	0.431	2.68	7.4	13.6	...	7012	3.3e4	2.3e4	4.8e6	41.8	32.0	1.7e3
G29.2−0.0	29.205	−0.047	2.22	5.4	10.9	...	6268	3.3e4	1.6e4	...	49.2	29.1	...
G30.1−0.2	30.069	−0.160	0.95	4.4	8.5	...	5897	2.8e4	2.9e4	...	61.9	62.1	...
G30.2−0.1	30.227	−0.145	2.59	4.4	6.3*	8.4*	9100	1.0e5	4.8e4	...	147.2/127.5	83.7/72.5	...
G30.3−0.0	30.277	−0.020	0.73	4.4	6.2	...	5896	2.5e4	2.6e4	2.2e6	70.5	72.5	2.0e3
G30.4−0.2	30.404	−0.238	3.59	4.3	8.0	...	5859	7.0e4	9.9e4	...	90.5	117.6	...
G30.5−0.3	30.502	−0.290	2.96	4.3	7.3	...	5860	4.3e4	7.9e4	...	68.7	108.2	...
G30.5+0.4	30.467	0.429	2.13	5.7	3.6*	11.0*	6194	2.0e4	2.1e4	...	59.8/34.2	61/34.8	...
G30.6−0.1	30.602	−0.106	2.40	4.4	7.3	...	6800	1.2e5	8.7e4	...	158.2	123.5	...
G30.7−0.3	30.694	−0.261	3.27	4.5	8.3	...	6800	1.8e5	6.7e4	...	185.4	87.3	...
G30.8−0.0	30.776	−0.029	62.17	4.6	5.7	...	7030	8.6e5	1.4e5	4.2e8	345.2	88.6	2.9e4
G31.0+0.5	31.050	0.480	1.75	7.1	12.9	...	6901	6.3e4	2.1e4	5.5e6	77.8	34.6	2.2e3
G31.1+0.3	31.130	0.284	1.11	4.4	7.3	...	5896	7.4e4	2.8e4	7.5e6	132.7	64.2	4.2e3

Notes. Quoted fluxes are from single-dish measurements by Altenhoff et al. (1979), Downes et al. (1980), and Kuchar & Clark (1997). Galactocentric and solar distances are from AB09, based on Lockman (1989) RRL observations. Solar distances denoted with * are computed from radial velocities in Lockman (1989) combined with the rotation curve by McClure-Griffiths & Dickey (2007). D_f denotes the far distance solution for sources with unresolved distance ambiguity. Details on the derivation of T_e, EM, and n_e can be found in Section 3. $EM_{6\,cm}$ and $EM_{20\,cm}$ are, respectively, the emission measure computed from single-dish and MAGPIS fluxes. $n_{e,6\,cm}$ and $n_{e,20\,cm}$ are the corresponding electron densities. EM_{shell} and $n_{e,shell}$ denote the emission measure and electron density estimated by assuming that the source is characterized by a shell-like geometry.

Table 2
Angular and Linear Diameters

Name	θ (arcmin)	d (pc)	θ_{maj} (arcmin)	θ_{min} (arcmin)	d_{maj} (pc)	d_{min} (pc)	θ_{shell} (arcsec)	d_{shell} (pc)
G28.8−0.2	2.2	3.5	3.0	3.0	4.8	4.8	...	...
G29.0−0.6	2.3	2.3	3.5	3.0	3.4	3.0	6	0.1
G29.1−0.0	4.3	14.4	3.3	2.1	11.0	7.0	...	...
G29.1+0.4	4.8	19.0	9.7	3.4	38.4	13.4	12	0.8
G29.2−0.0	4.3	13.6	9.1	4.1	28.8	13.0	...	...
G30.1−0.2	3.0	7.4	3.9	2.3	9.6	5.7	...	...
G30.2−0.1	2.6	4.7/6.3	4.1	3.5	7.5/10.0	6.4/8.5	...	...
G30.3−0.0	2.8	5.0	3.6	2.1	6.5	3.8	9	0.3
G30.4−0.2	3.7	8.6	4.6	2.1	10.7	4.9	...	...
G30.5−0.3	4.3	9.1	5.6	1.8	11.9	3.8	...	...
G30.5+0.4	5.4	5.6/17.3	5.6	5.1	5.9/17.9	5.3/16.3	...	...
G30.6−0.1	2.3	4.9	3.2	2.3	6.8	4.9	...	...
G30.7−0.3	2.2	5.3	4.4	3.0	10.6	7.2	...	...
G30.8−0.0	4.4	7.2	13.8	8.6	22.9	14.2	6	0.2
G31.0+0.5	2.8	10.5	5.5	4.2	20.6	15.8	9	0.6
G31.1+0.3	2.0	4.2	3.1	3.4	6.6	7.2	6	0.2

Notes. The angular diameter θ and corresponding linear diameter, d, are obtained from the single-dish measurements by Altenhoff et al. (1979), Downes et al. (1980), and Kuchar & Clark (1997), while θ_{maj}, θ_{min}, d_{maj}, and d_{min} are derived from the MAGPIS data (Section 3 and Figure 9). All linear diameters are estimated with the heliocentric distances quoted in Table 1. θ_{shell} and d_{shell} denote the shell angular size and linear thickness in the hypothesis of a shell-like geometry of the source.

and MAGPIS measurements ($EM_{20\,cm}$, Column 10), emission measure obtained assuming shell-like geometry of the source (EM_{shell}, Column 11), electron density computed from single-dish ($n_{e,6\,cm}$, Column 12) and MAGPIS measurements ($n_{e,20\,cm}$, Column 13), and electron density computed assuming shell-like geometry of the source ($n_{e,shell}$, Column 14). Table 2 provides additional information on angular sizes (θ) and linear diameters (d).

Six centimeter fluxes and angular diameters are from Altenhoff et al. (1979), Downes et al. (1980), and Kuchar & Clark (1997). Galactocentric and solar distances are, for all the sources with the exception of three cases (G29.0−0.6, G30.2−0.1, G30.5+0.4), from Anderson & Bania (2009, hereafter AB09), based on Lockman (1989) RRL observations. For these sources, AB09 solved the kinematic distance ambiguity, using H I emission/absorption and self-absorption data. We adopted their recommended values. In the case of G29.0−0.6, AB09 suggested that the source is situated at the far distance (11.5 kpc), although they obtained contradictory results from the H I emission/absorption data (near solution) with respect to

the self-absorption data (far solution). In their paper, the authors stated that the H I emission/absorption measurements are usually more reliable for discriminating between near and far solutions. However, for this specific source, the self-absorption data are of better quality, so they assigned it to the far distance. We visually inspected the ^{13}CO data from the Galactic Ring Survey (Simon et al. 2001) and noted that G29.0−0.6 appears to form a coherent structure with a companion source, G29.1−0.7, for which the likely source of ionization (the B1 II type star S65−4) has a known photometric distance of 3.6 kpc (Forbes 1989). For this reason, we re-located G29.0−0.6 to the near distance (3.4 kpc). For two sources (G30.2−0.1 and G30.5+0.4) AB09 did not solve the distance ambiguity. For these, we computed the Galactocentric and solar distances using the McClure-Griffiths & Dickey (2007) rotation model, taking $R_0 = 8.5$ kpc and $\theta_0 = 220$ km s^{-1}, combined with the Lockman (1989) RRL measurements. The near and far solar distances for these two sources are quoted in Table 1 and both are used for the derivations of d, T_e, EM, and n_e. For four sources, the value of T_e reported in the table is from Downes et al. (1980—G30.2−0.1, G30.6−0.1, G30.7−0.3) and Quireza et al. (2007—G30.8−0.0). For the other sources, a crude estimate of T_e is obtained by applying the relation (Deharveng et al. 2000)

$$T_e = (372 \pm 38)R + (4260 \pm 350). \quad (1)$$

For all the sources EM is computed from Mezger & Henderson (1967):

$$T_b = 8.235 \times 10^{-2} a T_e^{-0.35} \nu^{-2.1} \mathrm{EM}. \quad (2)$$

In Equation (2), T_b (the observed brightness temperature) and T_e are in K, ν is in GHz, and a is a constant set equal to 1. EM, combined with the linear diameter, is used to derive n_e from

$$n_e = \sqrt{\frac{\mathrm{EM}}{d}}. \quad (3)$$

In the expression above, we assumed that n_e is uniform across the source and that this is spherically symmetric. However, most of the sources in our sample do not have a spherical morphology. In Section 6, we will return on this point and discuss its implications. Because EM has a weak dependence on T_e (EM $\propto T_e^{-0.35}$), we do not expect the application of the empirical relation in Equation (1) to bias significantly the derivation of this quantity and, in turn, of the electron density. We note that all the emission measures quoted in Table 1 are of the order of 10^2 cm^{-3}, suggesting that our sample is homogeneous and consists only of evolved H II regions.

Finally, we computed, from the single-dish measurements, the Ly(α) luminosity of each source:

$$L(\mathrm{Ly}\alpha) = 3.20 \times 10^2 \left(\frac{S_\nu}{\mathrm{Jy}}\right)\left(\frac{T_e}{10^4\ \mathrm{K}}\right)^{-0.45} \cdot \left(\frac{\nu}{\mathrm{GHz}}\right)^{0.1}\left(\frac{D}{\mathrm{kpc}}\right)^2 L_\odot \quad (4)$$

(Garay et al. 1993) and the number of ionizing photons needed to excite the H II region:

$$N_{\mathrm{Lyc}} = 6.3 \times 10^{52}\ \mathrm{photons\ s^{-1}} \left(\frac{T_e}{10^4\ \mathrm{K}}\right)^{-0.45} \cdot \left(\frac{\nu}{\mathrm{GHz}}\right)^{0.1} \frac{L_\nu}{10^{27}\ \mathrm{erg\ s^{-1}\ Hz^{-1}}} \quad (5)$$

(Condon 1992). In the relations above, $L_\nu = S_\nu 4\pi D^2$, and S_ν, D, and T_e are, respectively, the 6 cm flux, heliocentric distance, and electron temperatures that appear in Columns 4, 6/7, and 8 of Table 1. L(Lyα) and N_{Lyc} are reported in Table 6. The sources in our sample have ionizing luminosities in the range $\sim 10^{48}$–10^{50} photons s^{-1}, with a mean value of $10^{49.1\pm0.54}$ photons s^{-1}. According to Smith et al. (1978), H II regions with an ionizing luminosity at least four times greater than the Orion Nebula (i.e., 4×10^{49} photons s^{-1} at $R_0 = 10$ kpc) are defined as *giant*. When properly re-scaled by a factor of 0.85 for $R_0 = 8.5$ kpc (McKee & Williams 1997), the threshold for giant H II regions becomes equal to 3.4×10^{49} photons s^{-1}, indicating that our sample consists of two giant H II regions (G29.1+0.4 and G30.8−0.0) and 14 sub-giant ones, many of which (at least 7) are close to the giant regime.

4. SEDs

4.1. Evaluating the SEDs

The single-dish archival data used to establish the evolutionary stage of our sources have too coarse a spatial resolution for allowing the accurate definition of the boundaries of the ionized-gas-dominated region within each source. To this end, we made use instead of the MAGPIS 20 cm data, which are characterized by an angular resolution of 6″, i.e., comparable to the PACS 70 μm resolution. For each H II region, we drew MAGPIS contours at 3σ above the background level and used these to evaluate the extent of the actual H II region.

The IR wavelengths that we are considering, as well as being contributed to by dust emission, are contaminated, especially in the PACS and SPIRE bands, by additional free–free (e.g., thermal bremstrahlung) emission. To evaluate this contribution, we need to take into account the dependence on both frequency and electron temperature of the free–free spectral index, β_{ff} ($S \sim \lambda^{\beta_{ff}}$). This is because the canonical approximation $\beta_{ff} = 0.1$ holds true only up to 10 GHz (3 cm) and electron temperatures of the order of 8000 K. At higher frequencies (shorter wavelengths) and lower electron temperatures, the spectral index can differ from this value by a few to tens of a percent. Therefore, to each source we applied the relation (Bennett et al. 1992)

$$\beta_{\mathrm{ff},\lambda} = [11.68 + 1.5 \ln(T_e/8000\ \mathrm{K}) + \ln(\lambda/m)]^{-1}. \quad (6)$$

We used the values of T_e reported in Table 1, together with the assumption that the abundance of ionized He (He++) is negligible with respect to the abundance of ionized H (H+). Table 3 provides, for each source, β_{ff} in the range 24 μm–500 μm. We did not compute β_{ff} at 8 μm, since in the mid-IR free–free transitions become sub-dominant with respect to free-bound transitions and these, in turn, are negligible when compared to dust emission (Beckert et al. 2000). From Table 3, we see that, in the range 24–500 μm, β_{ff} varies between a minimum of 1.7 and a maximum of 0.2, thus the subtraction of the free–free contribution becomes relatively important (of the order of a few percent) only at the longer SPIRE wavelengths. For each source, the free–free-corrected flux at a given wavelength $\bar{\lambda}$, $\widetilde{S_{\bar{\lambda}}}$, was obtained by subtracting from the IR flux, $S_{\bar{\lambda}}$, the MAGPIS 20 cm flux re-scaled to $\bar{\lambda}$ using

$$\widetilde{S_{\bar{\lambda}}} = S_{\bar{\lambda}} - \sum_{\lambda=20\,\mathrm{cm}}^{\bar{\lambda}} S_{20\,\mathrm{cm}} * \left(\frac{20 \times 10^5}{\lambda}\right)^{\beta_{ff,\lambda}}, \quad (7)$$

Table 3
Free–Free Spectral Indices

Name	$\beta_{\rm ff,24}$	$\beta_{\rm ff,70}$	$\beta_{\rm ff,160}$	$\beta_{\rm ff,250}$	$\beta_{\rm ff,350}$	$\beta_{\rm ff,500}$
G28.8−0.2	1.67	0.60	0.40	0.34	0.30	0.27
G29.0−0.6	1.39	0.56	0.38	0.32	0.29	0.27
G29.1−0.0	1.39	0.56	0.38	0.32	0.29	0.27
G29.1+0.4	1.18	0.52	0.36	0.31	0.28	0.26
G29.2−0.0	1.47	0.57	0.39	0.33	0.30	0.27
G30.1−0.2	1.69	0.60	0.40	0.34	0.30	0.27
G30.2−0.1	0.80	0.43	0.32	0.28	0.25	0.23
G30.3−0.0	1.69	0.60	0.40	0.34	0.30	0.27
G30.4−0.2	1.72	0.60	0.40	0.34	0.31	0.28
G30.5−0.3	1.72	0.60	0.40	0.34	0.31	0.28
G30.5+0.4	1.51	0.58	0.39	0.33	0.30	0.27
G30.6−0.1	1.24	0.55	0.37	0.32	0.29	0.26
G30.7−0.3	1.24	0.53	0.37	0.32	0.29	0.26
G30.8−0.0	1.17	0.52	0.36	0.31	0.28	0.26
G31.0+0.5	1.21	0.52	0.37	0.31	0.28	0.26
G31.1+0.3	1.69	0.60	0.40	0.34	0.30	0.27

Notes. Free–free spectral indices ($\beta_{ff,\bar{\lambda}}$) at a fixed wavelength $\bar{\lambda}$ as a function of electron temperatures (see Table 1, Column 8).

with λ in μm. Of note, the single-dish fluxes quoted in Table 1, properly re-scaled to 20 cm using a canonical free–free spectral index 0.1, are within ∼20% of the MAGPIS measurements.

After free–free subtraction, using the apertures obtained from the 20 cm MAGPIS data, we estimated the flux and built the SEDs by combining the MIPS 24 μm (and when, necessary, the MIPS/*MSX* data) with the PACS and SPIRE data. We also tried to include the 1.1 mm data, at 33″ resolution, from the Bolocam Galactic Plane Survey (BGPS; Rosolowsky et al. 2010). However, the SED modeling revealed a significant flux loss at this wavelength (Figures 1 and 2). The origin of this effect can be attributed to the BGPS data processing, which largely (at more than 90% level) removes emission on scales of or greater than 5.′9. This operation is necessary in order to separate the astronomical signal from the atmospheric fluctuations in the data streams. For structures larger than 3.′8, the attenuation is of the order of 50% (Aguirre et al. 2011). The 16 H II regions in our sample have an average angular size of 3.′2, hence still in the range in which the extended emission should be preserved for the most part. Therefore, our result appears to indicate that the amount of filtered flux is more than expected, at least on the scales that we are considering. We could compensate for this effect by artificially increasing the systematic error. Instead, we opted for a more conservative approach and decided to exclude the 1.1 mm data from the fit. We note that the loss of signal on a large angular scale would have been comparable or even greater if, rather than the BGPS data set, we had used the 19″ resolution ATLASGAL (Schuller et al. 2009) data at 870 μm. In this case, a significant fraction of flux is removed from the data already on scales as small as 2.′5, which is smaller than the average size of the H II regions in our sample.

For 24 μm $< \lambda <$ 500 μm, the flux at each wavelength and for each H II region was determined within the defined apertures after point-source subtraction—performed with the Starfinder algorithm (Diolati et al. 2000)—and convolution to the SPIRE 500 μm angular resolution (35″). To evaluate the background level, we took the median within a control region, selected to be close to the source under consideration, yet paying attention to avoid potentially contaminating bright objects. Uncertainties on measured fluxes ($\widetilde{\sigma_S}$), prior to free–free subtraction, were obtained by adding in quadrature the calibration error and the background standard deviation, according to

$$\widetilde{\sigma_S} = \left(\sum_{i=1}^{N} \widetilde{\sigma_{S_i}}^2 + N^2 \sigma^2_{\overline{back}} \right)^{1/2}, \quad (8)$$

where $\widetilde{S_i}$ is the flux in pixel i, N is the number of pixels within the aperture, and $\overline{back}$ is the median background in the control region. To this error, due to the subtraction of the free–free contribution, we added in quadrature an extra 30% uncertainty associated with the MAGPIS data (e.g., Povich et al. 2007). We also removed the zodiacal light contribution from the 24 μm data. This operation was carried out using the entry "ZODY_EST" in the FITS header of each 24 μm frame, where the amount of zodiacal light per frame was estimated by the Spitzer Science Center from the predictions on Kelsall et al. (1998).

The photometric measurements performed after background subtraction retrieved, at every wavelength and for each source, a positive flux (see Table 4). The average signal-to-noise ratio (S/N) across all the bands and for the entire sample is $\overline{\rm S/N_{\lambda_{all}}} = 3.6 \pm 2.1$. If we break this number per wavelength, we have: $\overline{\rm S/N_{8\,\mu m}} = 4 \pm 2.3$, $\overline{\rm S/N_{24\,\mu m}} = 6.7 \pm 1.9$, $\overline{\rm S/N_{70\,\mu m}} = 3.3 \pm 0.9$, $\overline{\rm S/N_{160\,\mu m}} = 2.4 \pm 1$, $\overline{\rm S/N_{250\,\mu m}} = 2.9 \pm 1.6$, $\overline{\rm S/N_{350\,\mu m}} = 2.6 \pm 1.4$, and $\overline{\rm S/N_{500\,\mu m}} = 2.7 \pm 1.5$. We note that, as a general trend, the significance of the detection tends to decrease with increasing wavelength. This is likely due to the fact that at $\lambda \sim 160\,\mu$m, the emission from the H II region starts competing with the emission of the interstellar medium (ISM). At longer wavelengths (i.e., in SPIRE bands), this contribution becomes sub-dominant with respect to the local background.

It is worth mentioning that the detected IR emission that we ascribed entirely to H II regions could instead originate from warm/cold material located in the foreground/background along the line of sight. Indeed, this bias at least partly affects our flux extraction procedure. In fact, in the presence of a structured, highly varying background such as the one characterizing the Galactic plane, background subtraction does not assure the complete removal of emission unrelated to the source, due to the intrinsic difficulty of estimating the background level. However, what provides confidence in our results is the fact that, for the majority of the sources, the MAGPIS 20 cm emission, which traces the ionized gas component of our H II regions, does not (or not completely) overlap with the peak of the IR emission in the other bands (likely associated with the PDR), suggesting that the H II region and its dust content is largely (or partly) exposed to the observer.

4.2. SED Fitting

Figures 1 and 2 show the SEDs derived from the photometric measurements described in the previous section. Since the pioneering works of Chini et al. (1986a, 1986b, 1986c, 1987), it is known that, in order to explain observations of H II regions above and below ∼100 μm in the framework of traditional dust models, that is, with a constant spectral emissivity index $\beta_{\rm dust}$, it is necessary to invoke the existence of a two-temperature component dust distribution: a warm, low-density population of dust grains situated in the proximity of the ionizing source, and a colder dust population far from the central star (or stars). One has to keep in mind that the observations that Chini et al. used

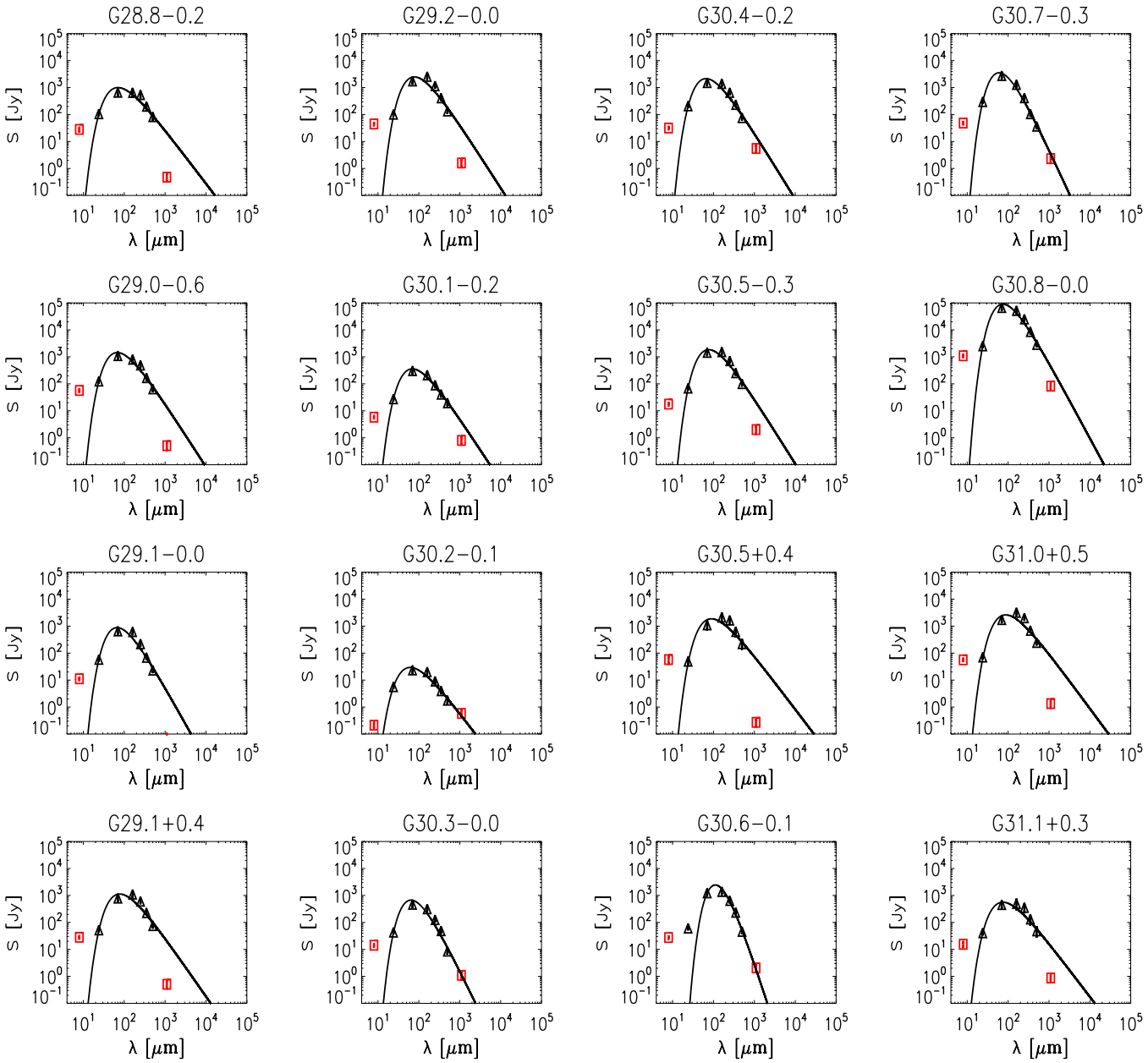

Figure 1. SEDs for all the H II regions in our sample. Triangles denote photometric measurements at 24 μm (MIPS), 70 μm and 160 μm (PACS), 250 μm, 350 μm, and 500 μm (SPIRE). Red squares indicate the IRAC 8 μm and Bolocam 1.1 mm data points. Also shown are photometric uncertainties. The solid line corresponds to the best-fit isothermal model with varying emissivity spectral index.

(A color version of this figure is available in the online journal.)

to constrain their modeling were taken in the early 1980s and, as such, were characterized by relatively low angular resolution, with the consequence that the actual H II region was not resolved with respect to the associated PDR.

Both laboratory experiments and observations conducted in recent years suggest that traditional dust models assuming a constant spectral emissivity index might need to be revised (see discussion below). For this reason, we tried to fit our SEDs in three possible ways: (1) with an isothermal modified blackbody with constant spectral emissivity index ($\beta_{\rm dust} = 2$); (2) with an isothermal modified blackbody with variable $\beta_{\rm dust}$; and (3) with a two-temperature component model with $\beta_{\rm dust} = 2$. We did not attempt the fit with a two-temperature component model with variable $\beta_{\rm dust}$ since the measurements would not provide enough constrains (six data points) with respect to the number of free parameters (six parameters). We also did not include in the fit the IRAC 8 μm band, to which emission associated with stochastically heated PAHs typically contributes. To properly take into account PAH emission, we would need, for each H II region in our sample, an accurate knowledge of the radiation field generated by the central source, and this information should be coupled to a sophisticated dust model (e.g., DustEM; Compiegne et al. 2011) able to reproduce, in a coherent way, both the aromatic features and the continuum thermal emission due to larger grains. Since detailed information on the radiation field is not available for most of our H II regions, we considered only the data at wavelengths longer than 24 μm. The three functional forms corresponding to our three

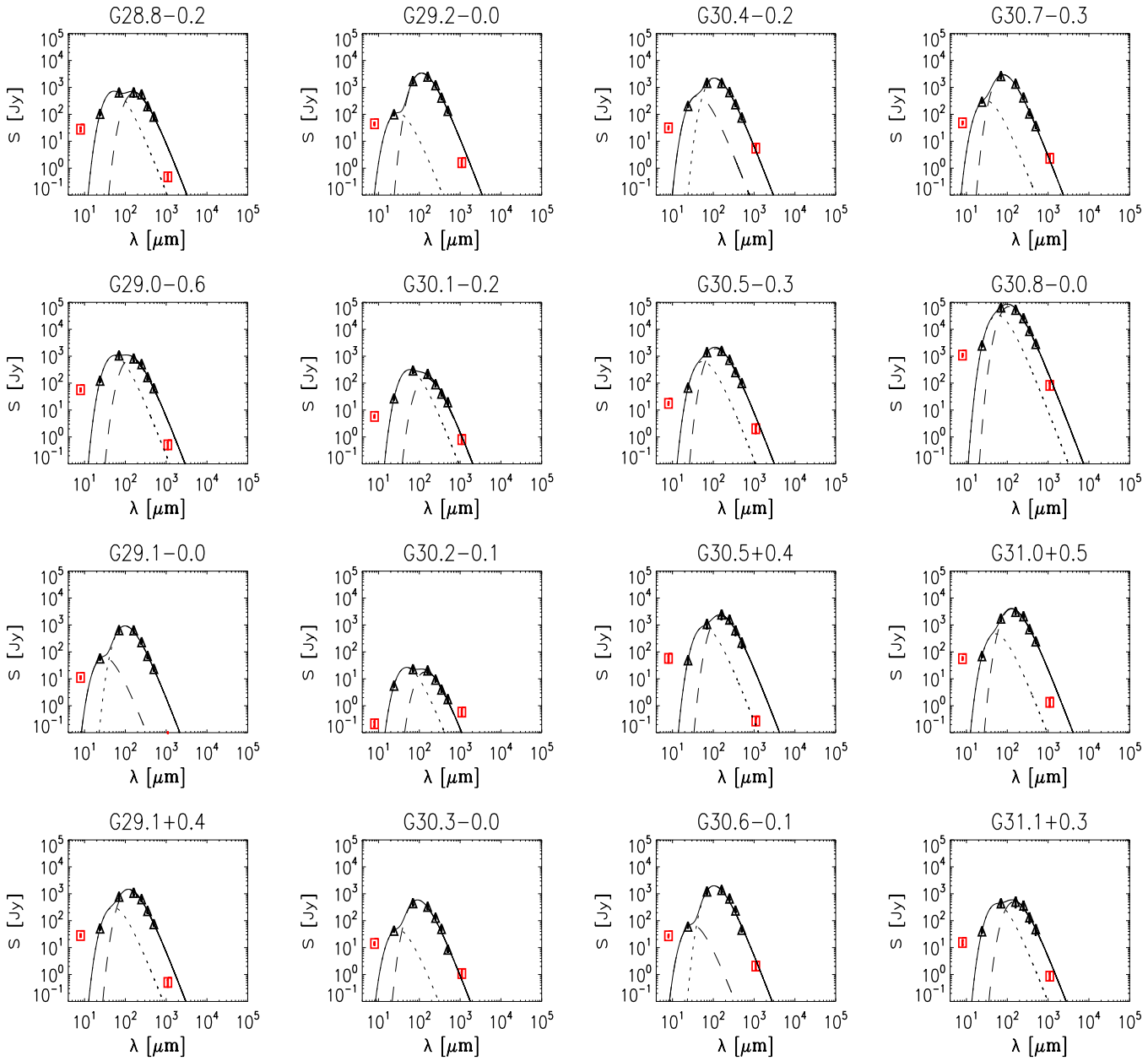

Figure 2. SEDs for all the H II regions in our sample. Triangles denote photometric measurements at 24 μm (MIPS), 70 μm and 160 μm (PACS), 250 μm, 350 μm, and 500 μm (SPIRE). Also shown are the IRAC 8 μm and Bolocam 1.1 mm data points (red squares) and photometric uncertainties. The solid line indicates the best-fit two-temperature dust component model with $\beta_{\rm dust} = 2$. Dashed lines illustrate the warm and cold components.

(A color version of this figure is available in the online journal.)

adopted models are

$$\widetilde{S_{\lambda,1}} = A_{1,1}\left(\frac{\lambda}{\lambda_0}\right)^{-2} B_\lambda(T_{\rm dust,1}) \quad (9)$$

for an isothermal model with constant emissivity index

$$\widetilde{S_{\lambda,2}} = A_{1,2}\left(\frac{\lambda}{\lambda_0}\right)^{-\beta_{\rm dust}} B_\lambda(T_{\rm dust,2}) \quad (10)$$

for an isothermal model with variable $\beta_{\rm dust}$, and

$$\widetilde{S_{\lambda,3}} = A_{1,3}\left(\frac{\lambda}{\lambda_0}\right)^{-2} B_\lambda(T_{c,3}) + A_{2,3}\left(\frac{\lambda}{\lambda_0}\right)^{-2} B_\lambda(T_{w,3}) \quad (11)$$

for a two-temperature component model, where $T_{c,3}$ and $T_{w,3}$ are, respectively, the temperatures of the cold and warm components, and λ_0 is set to 100 μm.

The choice of $\beta_{\rm dust} = 2$ is motivated by the fact that observations of the silicate absorption feature near 10 μm seem to indicate that big grains (BGs) are amorphous materials (Kemper et al. 2004), and these are expected to behave in a similar fashion to crystalline dielectric materials, for which sub-mm absorption has a temperature-independent quadratic dependence on frequency (Boudet et al. 2005).

To estimate the parameters $A_{1,1}$, $T_{\rm dust,1}$, $A_{1,2}$, $T_{\rm dust,2}$, $A_{2,3}$, $T_{c,3}$, and $T_{w,3}$ for each model (Equations (9)–(11)), we used a Monte Carlo Markov Chain (MCMC) method (Lewis & Bridle 2002). This technique consists in looking for the likelihood maximum by sampling the parameters space with a Metropolis–Hastings algorithm. The a priori probability densities of the parameters were set to be as wide as possible to avoid introducing artificial biases in the fit. Color corrections were computed iteratively

Table 4
Results of Photometric Measurements

Name	S_{24} (Jy)	b_{24} (MJy sr^{-1})	S_{70} (Jy)	b_{70} (MJy sr^{-1})	S_{160} (Jy)	b_{160} (MJy sr^{-1})	S_{250} (Jy)	b_{250} (MJy sr^{-1})	S_{350} (Jy)	b_{350} (MJy sr^{-1})	S_{500} (Jy)	b_{500} (MJy sr^{-1})	Area arcmin^2
G28.8−0.2	106 ± 12	45 ± 2	658 ± 173	722 ± 58	658 ± 201	1848 ± 227	568 ± 123	1594 ± 199	214 ± 51	715 ± 77	89 ± 20	255 ± 36	28
G29.0−0.6	126 ± 13	30 ± 1	1090 ± 250	588 ± 14	823 ± 203	1049 ± 56	525 ± 87	692 ± 65	181 ± 35	356 ± 23	71 ± 13	126 ± 11	10
G29.1−0.0	57 ± 6	45 ± 3	656 ± 131	746 ± 84	640 ± 128	1831 ± 305	240 ± 36	1592 ± 281	78 ± 12	717 ± 104	27 ± 4	263 ± 44	7
G29.1+0.4	52 ± 5	25 ± 1	791 ± 158	278 ± 16	1113 ± 223	577 ± 36	642 ± 96	268 ± 30	248 ± 37	192 ± 12	82 ± 12	66 ± 5	33
G29.2−0.0	102 ± 10	39 ± 3	1762 ± 352	601 ± 66	2581 ± 516	1405 ± 175	1234 ± 185	1123 ± 148	450 ± 68	525 ± 57	150 ± 23	190 ± 27	37
G30.1−0.2	28 ± 3	74 ± 4	300 ± 60	1431 ± 69	219 ± 44	3290 ± 313	95 ± 16	2611 ± 329	44 ± 8	1070 ± 132	21 ± 4	398 ± 64	9
G30.2−0.1	6 ± 1	77 ± 3	23 ± 5	1265 ± 69	21 ± 4	2707 ± 146	10 ± 2	2171 ± 110	4 ± 1	927 ± 49	2 ± 1	333 ± 19	14
G30.3−0.0	43 ± 4	66 ± 2	457 ± 91	1169 ± 60	329 ± 66	2722 ± 181	136 ± 21	2186 ± 149	54 ± 8	908 ± 55	10 ± 2	318 ± 22	8
G30.4−0.2	209 ± 21	55 ± 5	1494 ± 299	934 ± 81	1450 ± 290	2203 ± 120	703 ± 105	1779 ± 69	259 ± 39	772 ± 26	85 ± 13	282 ± 11	10
G30.5−0.3	69 ± 7	69 ± 5	1429 ± 286	1137 ± 117	1582 ± 317	2538 ± 198	769 ± 115	1986 ± 155	281 ± 42	850 ± 68	113 ± 17	307 ± 25	10
G30.5+0.4	50 ± 12	34 ± 2	1114 ± 351	330 ± 38	2508 ± 877	934 ± 122	1901 ± 571	894 ± 111	732 ± 246	439 ± 42	262 ± 93	162 ± 1	29
G30.6−0.1	62 ± 6	89 ± 7	1237 ± 247	1554 ± 38	1407 ± 281	3915 ± 125	689 ± 103	3351 ± 104	259 ± 39	1364 ± 41	52 ± 8	497 ± 18	7
G30.7−0.3	299 ± 30	75 ± 4	2700 ± 540	1473 ± 62	1369 ± 274	3398 ± 164	456 ± 69	2813 ± 161	120 ± 19	1153 ± 72	42 ± 7	419 ± 28	13
G30.8−0.0	2545 ± 254	59 ± 9	65867 ± 13173	1148 ± 84	53229 ± 10647	3541 ± 264	26784 ± 4019	3162 ± 256	9358 ± 1406	1302 ± 108	3150 ± 475	474 ± 44	119
G31.0+0.5	71 ± 7	32 ± 1	1774 ± 355	436 ± 42	3198 ± 640	926 ± 100	2132 ± 320	872 ± 79	745 ± 112	436 ± 29	267 ± 40	161 ± 10	23
G31.1+0.3	41 ± 5	48 ± 1	451 ± 124	808 ± 41	511 ± 198	2362 ± 86	377 ± 128	2284 ± 91	143 ± 54	995 ± 31	53 ± 20	368 ± 13	11

Notes. For details on background level estimation and photometric uncertainties, see Section 3. The area quoted in Column 14 provides an estimate of the extraction aperture derived from the MAGPIS 20 cm data.

Table 5
Best-fit SED Parameters

Name	$T_{\rm dust,2}$ (K)	$\sigma_{T_{\rm dust,2}}$ (K)	$\beta_{\rm dust}$	$\sigma_{\beta_{\rm dust}}$	${\chi_{1t}}^2$	$\rm CDF_{1t}$	$T_{c,3}$ (K)	$\sigma_{T_{c,3}}$ (K)	$T_{w,3}$ (K)	$\sigma_{T_{w,3}}$ (K)	${\chi_{2t}}^2$	$\rm CDF_{2t}$
G28.8−0.2	72.66	10.26	1.2×10^{-4}	0.33	9.58	0.98	17.73	0.50	55.92	1.25	0.86	0.35
G29.0−0.6	65.81	9.87	3.6×10^{-1}	0.36	8.93	0.97	21.27	0.80	54.17	0.96	0.95	0.38
G29.1−0.0	58.98	13.89	7.3×10^{-1}	0.73	16.40	1.0	29.46	0.49	96.31	9.52	1.54	0.54
G29.1+0.4	60.96	7.65	1.8×10^{-1}	0.41	22.93	1.0	23.40	0.90	57.12	15.59	0.35	0.16
G29.2−0.0	57.15	4.82	3.7×10^{-1}	0.32	24.29	1.0	25.62	0.40	98.06	11.83	0.41	0.19
G30.1−0.2	65.04	2.14	3.2×10^{-1}	0.09	2.91	0.59	19.81	0.89	51.49	0.72	2.34	0.69
G30.2−0.1	82.45	1.12	1.0×10^{-2}	0.11	7.34	0.94	20.63	0.89	60.14	1.81	1.11	0.42
G30.3−0.0	55.01	8.79	1.1	0.50	24.49	1.0	31.91	1.01	98.37	10.54	7.16	0.97
G30.4−0.2	65.56	16.24	4.6×10^{-1}	0.67	17.76	1.0	26.70	0.93	70.55	12.00	0.15	0.08
G30.5−0.3	56.93	12.37	4.2×10^{-1}	0.62	11.83	0.99	24.65	1.10	53.00	11.69	0.92	0.37
G30.5+0.4	57.25	7.00	8.0×10^{-4}	0.38	8.73	0.97	18.95	0.55	48.55	0.98	0.40	0.18
G30.6−0.1	22.60	1.36	2.75	0.21	102.20	1.0	27.95	0.38	95.07	11.84	0.79	0.98
G30.7−0.3	56.15	1.83	1.31	0.11	9.11	0.97	36.15	0.92	97.33	10.79	2.98	0.77
G30.8−0.0	51.61	4.63	8.2×10^{-1}	0.25	10.29	0.98	25.94	1.08	50.33	16.81	0.40	0.18
G31.0+0.5	56.84	3.58	6.0×10^{-2}	0.28	28.07	1.0	22.58	0.60	56.10	7.18	1.22	0.46
G31.1+0.3	68.16	18.55	3.0×10^{-5}	0.71	4.28	0.77	19.72	0.64	52.33	1.02	0.23	0.11

Notes. Results obtained by fitting the 24 μm $< \lambda <$ 500 μm data points. $T_{\rm dust,2}$, $\sigma_{T_{\rm dust,2}}$ and ${\chi_{1t}}^2$ are the best-fit parameters and corresponding χ^2 for a one-temperature component model with variable $\beta_{\rm dust}$. $T_{c,3}$, $\sigma_{T_{c,3}}$, $T_{w,3}$, $\sigma_{T_{w,3}}$, and ${\chi_{2t}}^2$ are the best-fit parameters and χ^2 for a two-temperature (warm and cold) component model with $\beta_{\rm dust}$ equal to 2. $\rm PDF_{1t}$ and $\rm PDF_{2t}$ are the probability density functions associated with each model.

during the fitting procedure using the MIPS, PACS, and SPIRE transmission filters. In addition, systematic (i.e., calibration) uncertainties were taken into account and included in the parameters error bars by means of a dedicated Monte Carlo run. A straightforward χ^2 goodness-of-fit method was applied in parallel with the MCMC method to test the quality of the fits. In general, the best-fit values recovered by the two methods (MCMC and χ^2 goodness of fit) were found in agreement within a few percent.

The MCMC results of the fitting procedure for the isothermal model with varying spectral emissivity index and the two-temperature component model are given in Table 5. We do not show the results of the isothermal model with fixed $\beta_{\rm dust}$ as this model fails to reproduce simultaneously the 24 μm–500 μm observations. For the remaining two models, we made trial fits by including/excluding the 1.1 mm BGPS measurements. In both cases, the best-fit parameters (i.e., the best χ^2) were obtained by excluding the 1.1 mm Bolocam-extracted flux, as discussed in the previous section. A direct comparison between the isothermal and two-temperature component models in terms of χ^2 could not be performed, since the degrees of freedom are not constant. However, a comparison in terms of the cumulative density functions (CDFs)[10] for the χ^2 distribution of each model revealed, for all the sources but three, that the two-temperature component model is significantly more in agreement with the observations (see Columns 7 and 13 in Table 5). For G30.1−0.2, the one-temperature model seems to work surprisingly better than the two-temperature one, although the best-fit $\beta_{\rm dust}$ (0.32) lies outside the normally accepted range of values. In the case of G30.3−0.0 and G30.6−0.1 none of the models appears to be a good representation of the measured SEDs. For the 13 sources for which the two-temperature dust component model is in agreement with the data, we obtain that the cold component peaks between 100 μm and 160 μm and is characterized by a temperature in the range ∼20–30 K, while the warm component has a peak around 20 μm–70 μm with a temperature from ∼50 to ∼90 K. The average values for the cold and warm components are, respectively, $\overline{T_{c,3}} = 24.53 \pm 5.1$ K and $\overline{T_{w,3}} = 68.43 \pm 20.52$ K. We note that $\overline{T_{c,3}}$ does not differ significantly from temperatures measured in PDRs associated with wind-blown bubbles (WBBs; e.g., Rodon et al. 2010; Anderson et al. 2010). In principle, both cold and warm components could be attributed to BGs. This is indeed possible only if the warm and cold dust emissions are not spatially correlated, since a scenario in which two populations of large grains, subject to the same radiative field, thermalize at very different temperature is rather unrealistic. An alternative solution, for spatially coincident components, would be to assign the cold component to a population of BGs, and the warm component to a population of very small grains (VSGs). This option would be in agreement with the increase of VSG abundance in ionized environments reported (see Section 5) by Paradis et al. (2011) and Flagey et al. (2011), and which can be explained through partial sputtering of the BGs in the most inner parts of the H II regions. Without a more refined dust modeling that can take into account the radiation field properties of the sources, we cannot unambiguously conclude on this point.

For the two-temperature component model, we used a constant $\beta_{\rm dust}$. However, an increasing amount of evidence obtained both from laboratory experiments (Agladze et al. 1996; Mennella et al. 1998; Boudet et al. 2005) and observations targeting the cosmic microwave background (Dupac et al. 2003; Desert et al. 2008; Paradis et al. 2010; Veneziani et al. 2010) appears to support a temperature dependence (as well as a wavelength dependence, e.g., Paradis et al. 2011b) of the spectral emissivity index. Theoretically, the existence of an inverse relation between dust temperature and $\beta_{\rm dust}$ could be interpreted in light of the model recently proposed by Meny et al. (2007). This model, which was built over the two-level system (TLS) theory first formulated by Phillips (1972) and Anderson et al. (1972), explains the observed $T_{\rm dust}$–$\beta_{\rm dust}$ anti-correlation as being due to both the disordered charge distribution characterizing amorphous materials and TLS (or *tunneling*) effects that occur on a quantum scale in the grains structure.

[10] The CDF (or 1 p-value) gives the probability that a random variable X with a given probability distribution will be found at a value less or equal than x.

To analyze the possibility of a variation of $\beta_{\rm dust}$ with temperature, we considered the cold component only, which we fitted with a modified blackbody. For the warm component, we do not have enough measurements to constrain the fit with three free parameters ($\beta_{\rm dust}$, $A_{2,3}$, $T_{w,3}$). Since for the majority of the sources (10 out of 16) the 70 μm flux seems to contribute to the cold component (Figure 2), we included all the measurements in the range 70 μm $< \lambda <$ 500 μm.

The major complication in investigating a potential inverse relation between the spectral emissivity index and dust temperature is that these two quantities are intrinsically degenerate in parameter space. In fact, their two-dimensional posterior probability has an elongated, slant shape, and is characterized by the same functional form of the anti-correlation that we are trying to identify in the data (Shetty et al. 2009). In order to overcome this issue, we adopted the following procedure. We first fitted the measured fluxes using the MCMC algorithm, which allowed us to recover the joint posterior distribution of the parameters, thus keeping under control their intrinsic degeneracy. We then applied a technique successfully tested on BOOMERanG data (Veneziani et al. 2010), consisting of estimating the $T_{\rm dust}$–$\beta_{\rm dust}$ relation through a Monte Carlo of the calibration errors. That is, for each iteration j (100 in total): (1) we fitted Equation (10) to each source and derived the best-fit values of the parameters; and (2) we then estimated the relation

$$\beta_{\rm dust} = A \times \left(\frac{T_{\rm dust}}{20\ {\rm K}}\right)^{\alpha} \quad (12)$$

by combining the results obtained for all the sources; (3) at the end of the 100th iteration, we had a set of 100 pairs of A_j and α_j values, one for each realization of the calibration error. By marginalizing over the calibration errors,[11] we obtained the final best guess for A and α: $A = 3.0 \pm 0.2$, $\alpha = -1.5 \pm 0.2$. At first sight, this result might seem to confirm the existence of an inverse relation between spectral emissivity index and temperature. However, several authors (Masi et al. 1995; Shetty et al. 2009) argued that the observed anti-correlation might be spurious and due to line-of-sight temperature mixing effects. To test this hypothesis, we performed a simple simulation. We generated a synthetic random distribution of isothermal (30 K) H II regions and ISM, for which we adopted a dust temperature of 17 K (Boulanger & Perault 1988b). For both the H II regions and the ISM, we took $\beta_{\rm dust} = 2$. With the same strategy described above, consisting in applying the MCMC technique for both fitting the sources SEDs and estimating the best-fit values, A and α, we obtained: $A = 3.1 \pm 0.1$, $\alpha = -1.1 \pm 0.1$. These values are very similar to the ones derived from the 16 evolved H II regions. If, instead of $\beta_{\rm dust} = 2$, we adopt a slightly lower value, such as $\beta_{\rm dust} = 1.7$, then the best-fit anti-correlation for the simulated sample almost perfectly overlaps with the inverse relation estimated from the real sample (see Figure 3). We interpret these results as a strong indication that the observed anti-correlation is, at least in this case, likely due to a line-of-sight temperature mixing effect.

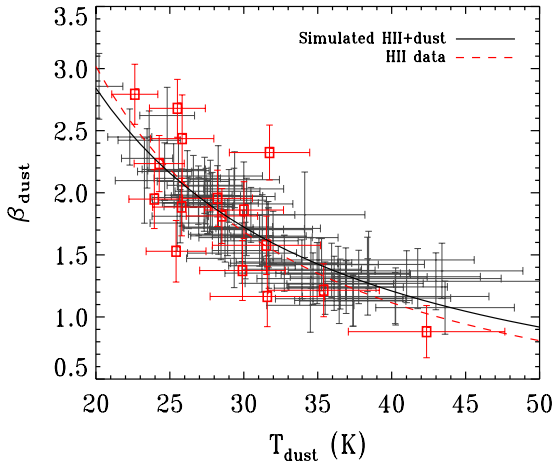

Figure 3. Simulated sample of a random distribution of H II regions and ISM (gray points and error bars) overlaid on the observed H II region sample (red points and error bars). The gray solid line is the best-fit function for the synthetic sample, while the red dashed line illustrates the best-fit model for the 16 H II regions considered in this work.

(A color version of this figure is available in the online journal.)

5. CAN DUST SURVIVE IN H II REGIONS?

The presence of dust in the warm ionized gas has been extensively debated in the literature, due to its relevance for our understanding of the processes of destruction and formation of dust grains in the ISM. Given the extreme conditions characterizing the interior of H II regions, theoretical models predict the depletion or partial destruction of the grains in these environments. Three main mechanisms could be responsible for this phenomenon (Inoue 2002): (1) radiation pressure, (2) stellar wind by the central source, and (3) dust sublimation. The effect of radiation pressure was investigated by Gail & Sedlmayr (1979), and more recently by Draine (2011). According to Gail & Sedlmayr (1979), radiation pressure is capable of generating a central zone of dust low density (or *cavity*) of size of the order of 20% the ionization radius. Gas cavities are instead known to be produced by stellar winds (Comeron 1997). However, given the coupling between dust and gas, a corresponding dust depletion zone is also expected. Sublimation appears to be the least effective process. In fact, if on one side, sublimation of dust grains could indeed occur as a consequence of the intense radiation field characterizing the most inner parts of an H II region, yet the estimated radius of the cavity induced by this mechanism is only of the order of 10^{-4} pc (Mookerjea & Ghosh 1999).

From the observational point of view, one of the main findings of Povich et al. (2007) is the significant decrease of PAHs inside M17, which is thought to be due to destruction of the aromatic molecules due to the extreme ultraviolet flux. Indication of PAH depletion associated with ionized gas is also reported by Paradis et al. (2011) for the Large Magellanic Cloud. These authors also found that the relative abundance of VSGs with respect to BGs appears to increase when transitioning from the neutral to the ionized medium. Flagey et al. (2011) arrived at a similar conclusion by analyzing the bright 24 μm emission filling up the interior of the M16 H II region, which they argued was caused by sputtering of BGs into VSGs. Finally, while the existence of BGs in neutral PDRs is supported by several studies (e.g., Povich et al. 2007; Compiegne et al. 2007), their survival in the interior of H II region is rather controversial and so far it is corroborated only by statistical analysis, such as cross-correlation of large data set tracing both IR and free–free emission (Lagache et al. 2000; Paladini et al. 2007; Planck Collaboration 2010).

[11] This operation is performed using the GetDist software of the public CosmoMC package.

6. IR EMISSION DISTRIBUTION INSIDE AND AROUND H II REGIONS

In this section, we address the question of *if* and what kind of dust is present in H II regions, and investigate the interplay between the neutral PDR and the inner H II region. Following the same procedure outlined in Section 4, we used the MAGPIS 20 cm contours to trace the ionized gas content of the inner H II region, and IRAC 8 μm, MIPS 24 μm, PACS 70 μm, and SPIRE 250 μm data to trace PAHs, VSGs, and BGs potentially associated with both the PDR and the H II region. With this radio/IR data set, we created two types of three-color images (Figure 4). The first set of images (left panels in Figure 4) is obtained by combining MAGPIS 20 cm (red), MIPS 24 μm (green), and IRAC 8 μm (blue) data, while the second set (right panels in Figure 4) is generated from the composite MAPGPIS 20 cm (red), SPIRE 250 μm (green), and PACS 70 μm (blue) data. A visual inspection of these figures reveals a wide range of morphologies of the sample H II regions, namely: bubbles (e.g., G28.8−0.2, G29.0−0.6, G31.1+0.3), elongated structures (e.g., G29.1+0.4, G30.5−0.3), diffuse nebulae (e.g., G30.1−0.2, G30.6−0.1), and more complex shapes (e.g., G30.8−0.0, G31.0+0.5).

Despite the complexity posed by dealing with different geometries, we identified three general trends in the color images: (1) the radio and 24 μm emission overlap in several cases, (2) the 8 μm and 70 μm emission are spatially correlated, and (3) the 250 μm emission distribution is frequently confused with the background level. In regions where the ISM emission is more attenuated, the peak of the 250 μm emission is often displaced with respect to the 20 cm peak, although one can find instances of partial overlap.

To investigate even further the relation between dust and ionized gas, we generated latitude and longitude emission profiles. For this purpose, we used MAGPIS 20 cm, IRAC 8 μm, MIPS 24 μm, and SPIRE 250 μm data. The profiles were obtained following these guidelines: (1) for each source and at each wavelength, we created a postage-stamp image, either $10' \times 10'$, $15' \times 15'$ or $20' \times 20'$, depending on the angular extent of the source; (2) we convolved the postage-stamp images at the same angular resolution (18″); (3) we regridded the images using a 6″ pixel size; (4) we generated the actual profiles by computing the median along each column (latitude cut) or row (longitude cut) of the convolved and regridded postage-stamp images; (5) at each wavelength we normalized each latitude/longitude profile to its maximum; and (6) finally, for every source, we overlaid the profiles at different wavelengths. The resulting profiles (see Figure 5) highlight the relative spatial distributions of the various components of dust emission already evidenced by the three-color images: the 8 μm and 250 μm emission peak almost exclusively outside the gas-dominated region, while the prominent emission at 24 μm appears to be closely associated with the H II region. To quantify this effect, we used the latitude and longitude profiles to measure the linear separation between the peaks of emission at different wavelengths. To this end, we excluded all ambiguous cases, i.e., H II regions for which the identification of the source with respect to the background, either in the latitude or longitude profile, is not straightforward. This is the case for G29.1−0.0, G29.2−0.0, and G31.1+0.3 (latitude profile), G30.1−0.2 (both latitude and longitude profiles), G30.5+0.4 (longitude profile). For the remaining sources, we computed from the profiles the angular distance of the IRAC 8 μm/SPIRE 250 μm/MIPS 24 μm peak of emission with respect to the MAGPIS 20 cm peak. With an estimate of the angular separation for each pair of wavelengths, we took the average of the values obtained from all the latitude and longitude profiles, and used the distance of the source to convert such an average into a linear distance (in parsecs). Figure 6 shows that the average linear separation between the peak of the 20 cm emission with respect to the peak of the 24 μm emission is half the distance between the peak of the same radio-continuum emission and the 8 μm emission and this, in turn, is also half the separation between the MAGPIS peak and the 250 μm one. If we assume, as customary, that the 8 μm data trace PAH emission and the 250 μm data trace BG emission, we can read this result as a strong indication that PAHs and BGs are not spatially correlated, with the PAHs statistically distributed along a ridge that appears to be closer to the ionizing source than the BGs ridge. This stratification is consistent with the scenario recently described in Draine (2011), in which radiation-pressure-driven drift is very effective in moving grains with a size $a > 0.01$ μm (BGs) outward, while smaller grains (PAHs) also drift, but do so more slowly. Remarkably, this is also in agreement with Krumholz & Matzner (2009) who claim that radiation pressure is usually unimportant for H II regions ionized by a small number of stars but becomes a dominant factor for the expansion dynamics of large H II regions. What remains as very puzzling is the source of the 24 μm emission. If this wavelength traced a population of VSGs coeval with respect to the BGs and PAHs at the periphery of the H II regions, we would expect from the predictions of Draine (2011) to find the emission peak between the 8 μm and the 250 μm peak. Likewise if the 24 μm emission was due to a coeval distribution of warm BGs. We then tentatively attribute this emission to a new generation of either VSGs or BGs. We note that this conclusion is similar to what was advocated by Everett & Churchwell (2010) from the analysis of the behavior of the 24 μm emission in WBB: that is, within bubbles, dust grains are re-supplied by destruction of embedded, dense cloudlets of interstellar material that are overrun by the expansion of the bubble itself.

The latitude and longitude profiles also show evidence that some of the sample H II regions are very prominent in emission at all wavelengths, while others are barely visible above the background level. This might indicate that different evolutionary stages are present in our sample. Although all of the H II regions that we are considering are evolved, some might be more evolved than others and, in particular, close to the stage where the internal pressure equalizes the external one, like, for instance, G30.1−0.2. Alternatively, as suggested by the recent MHD simulations by Arthur et al. (2011), highly irregular morphologies might be associated with highly ionized, density-bounded nebulae, powered by the hottest stars. Certainly, a mixture of both scenarios is also a possibility.

Both the three-color images and the profiles clearly show that the vast majority of the H II regions that we are analyzing are not characterized by spherical symmetry. Therefore, the angular diameters (and corresponding linear diameters) obtained from Gaussian fits of the single-dish data (Column 2 of Table 2) have to be considered only as a rough indication of the actual size of the sources. We then used the MAGPIS 20 cm contours to measure the angular size of each source along its major ($\theta_{\rm maj}$) and minor ($\theta_{\rm min}$) axes (Columns 4 and 5 of Table 2). The analysis of the latitude and longitude profiles also reveals that the 20 cm emission of six H II regions (G29.0−0.6, G29.1+0.4, G30.3−0.2, G30.8−0.0, G31.1+0.5, G31.5+0.3) is characterized by a double-peak behavior, suggesting that these

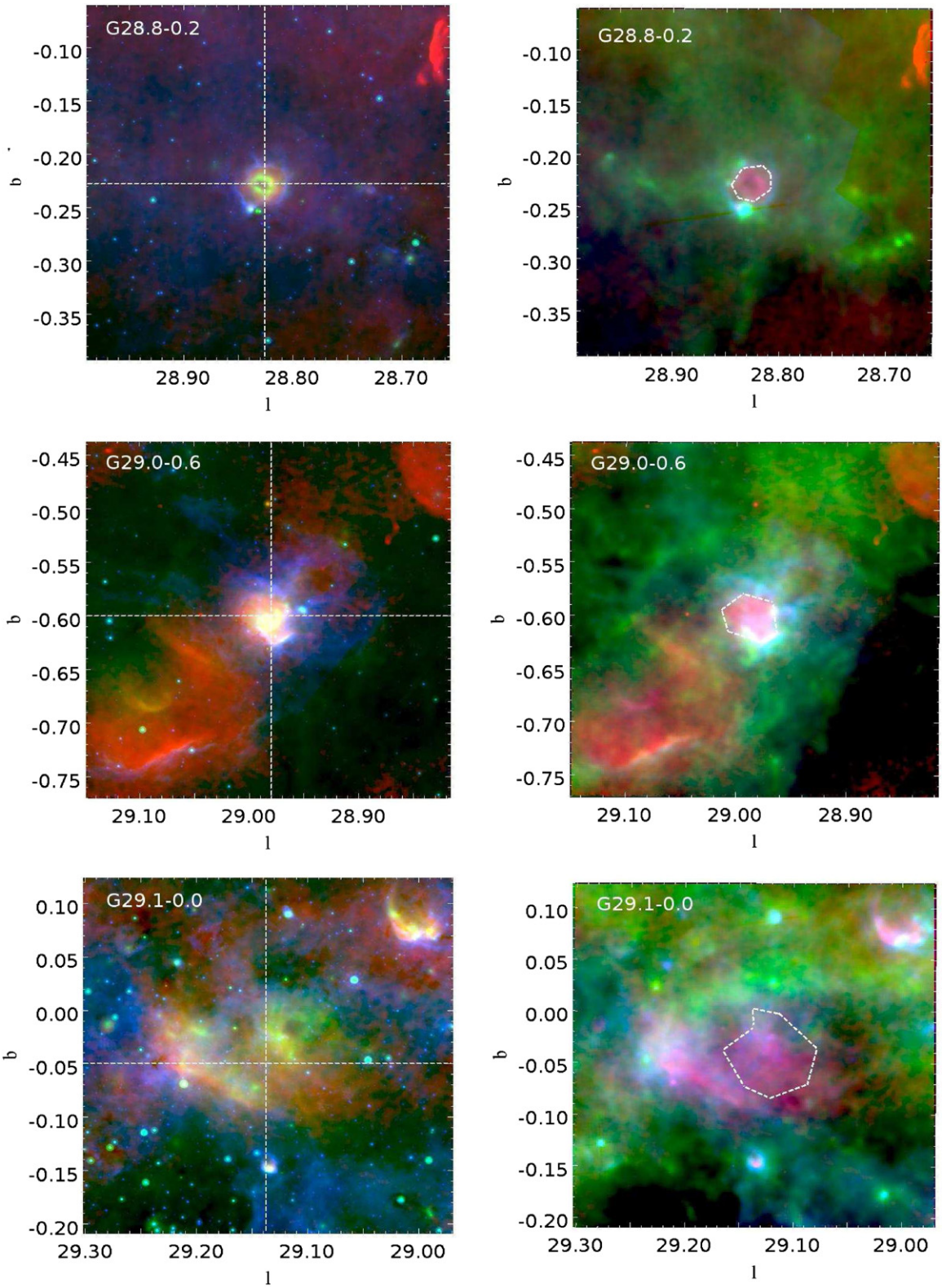

Figure 4. Three-color images of the sample evolved H II regions. Left panel: MAGPIS 20 cm (red), MIPS 24 μm (green), IRAC 8 μm (blue) data. Dashed lines indicate cuts in latitude and longitude operated to create the profiles in Figure 5. Right panel: MAGPIS 20 cm (red), SPIRE 250 μm (green), PACS 70 μm (blue) data. G29.1−0.0 and G29.2−0.0 are shown in the same panel (third row). Areas enclosed by white dashed lines denote approximate apertures using MAGPIS 20 cm data.
(A color version of this figure is available in the online journal.)

objects might present a shell-like geometry. If this was the case, the electron densities derived by assuming that a much larger volume is occupied by the ionized gas would be highly underestimated. Therefore, we computed the electron densities from the MAGPIS measurements both in the hypothesis of uniformly filled sources (case A) and by assuming a shell-like structure for the six H II regions showing a double-peak profile (case B). For case A, electron densities were obtained

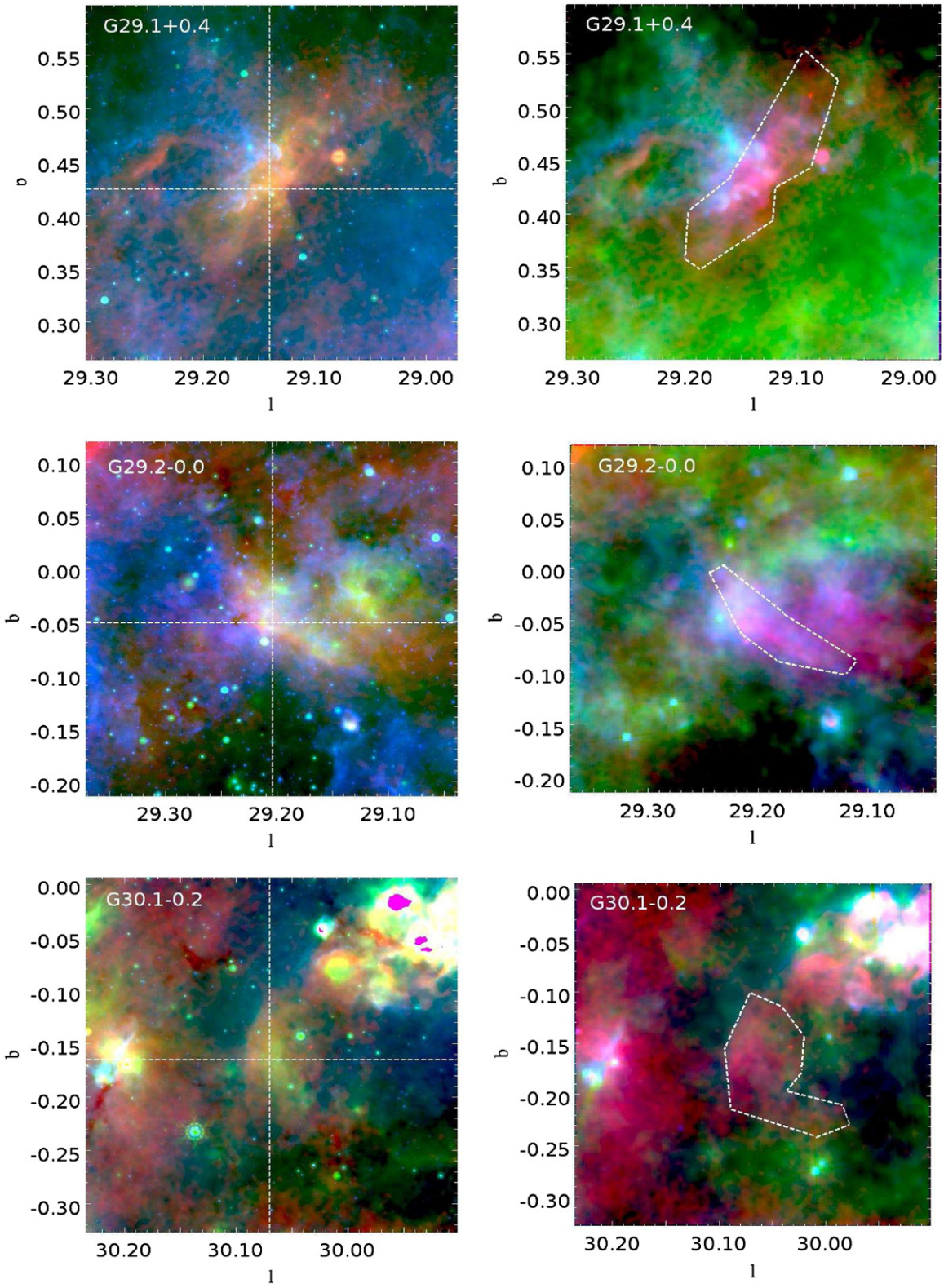

Figure 4. (Continued)

using the geometric mean, d_g[12], of the linear diameters $d_{\rm maj}$ and $d_{\rm min}$ inferred from the MAGPIS angular major and minor axes. For case B, we estimated the angular size of the shell from one of the peaks of the 20 cm double-peak profile (Column 8 of Table 2) and we converted this value into a shell thickness ($d_{\rm shell}$, see Column 9 in Table 2) using the heliocentric distance of the source. To evaluate the electron density, we doubled the estimated $d_{\rm shell}$, in order to account for the double crossing of

[12] $d_g = \sqrt{d_{\rm maj} \times d_{\rm min}}$.

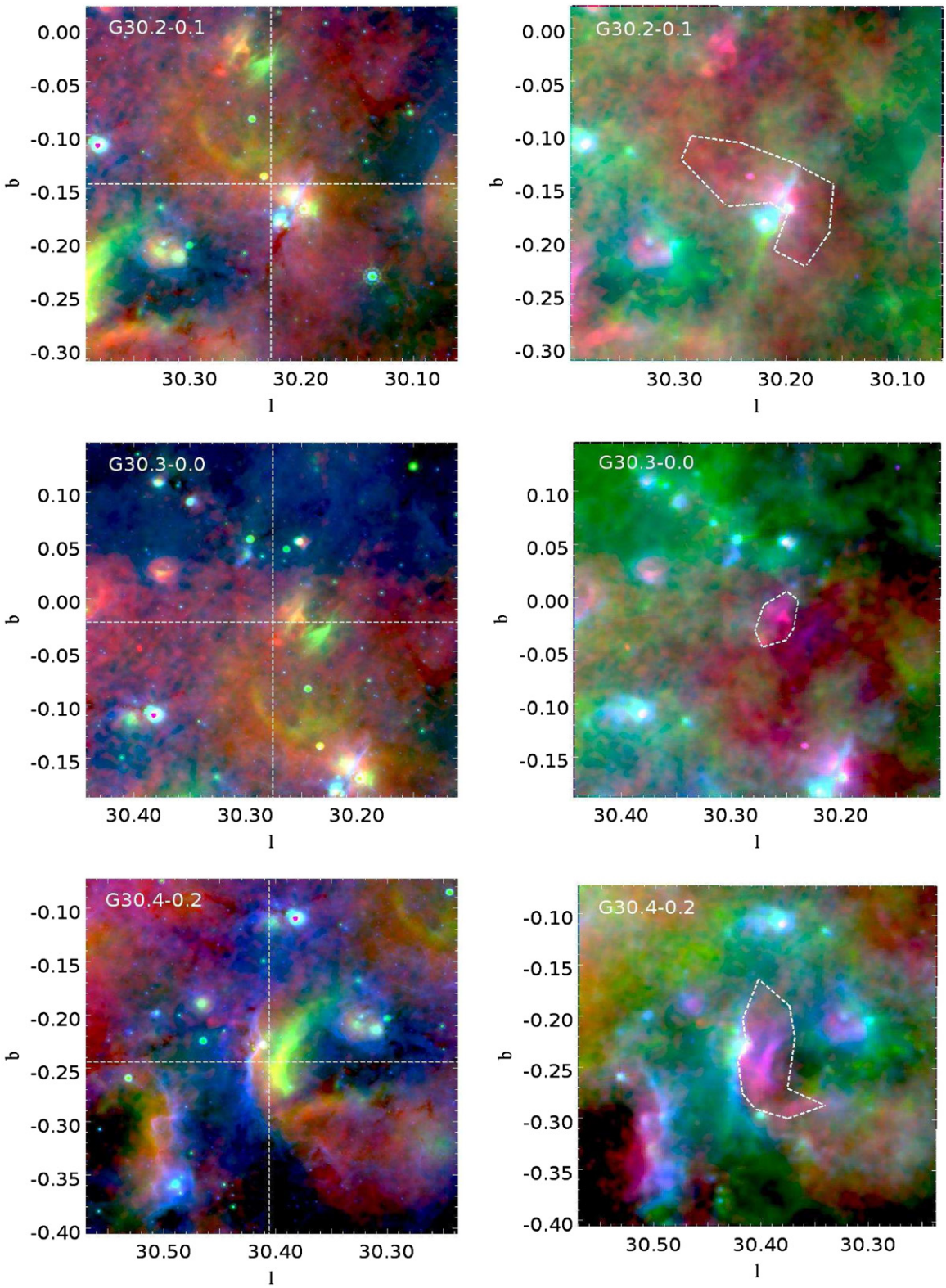

Figure 4. (Continued)

the shell with respect to the line of sight. The electron densities obtained for cases A and B are provided in Table 1.

With the derived electron densities and linear sizes, we explored the n_e–d relation. For a uniform-density nebula, n_e is expected to scale with the linear diameter as $d^{-3/2}$. Departures from this behavior can be explained by either invoking a non-uniform, clumpy nature of H II regions (Garay & Lizano 1999; Kim & Koo 2001) or the presence of dust particles in the ionize gas, which would absorb part of the ionizing radiation and would cause the H II region to be smaller. Here, for completeness, we considered the values of n_e and d estimated both from the single-dish and MAGPIS data, and from both cases

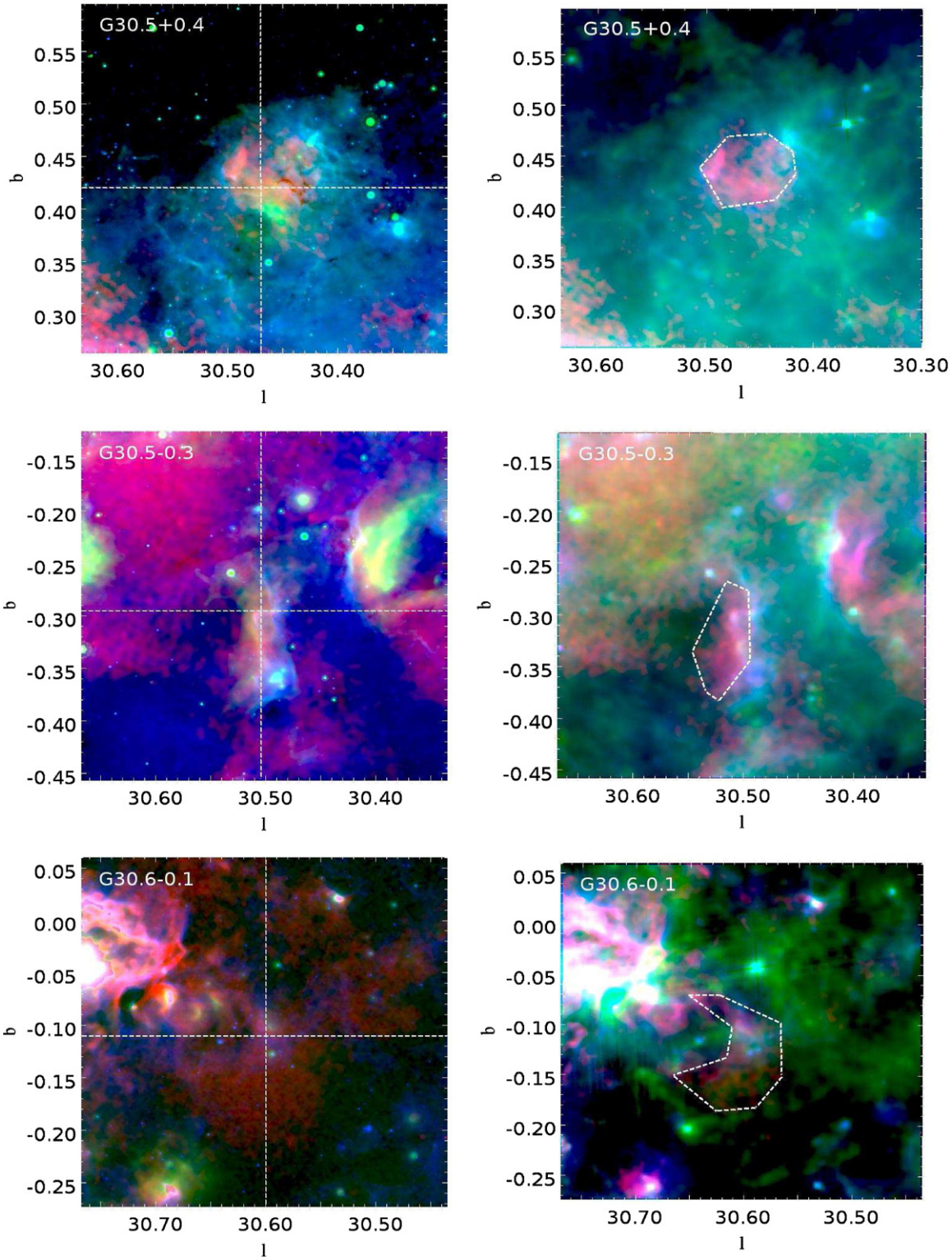

Figure 4. (Continued)

A and B. Figure 7 shows the best-fit model for, respectively, (1) the single-dish measurements assuming that the ionized gas uniformly fills the source volume (green dots); (2) the MAGPIS measurements with the same approximation as in (1) (blue dots); and (3) the MAGPIS measurements considering the potential shell-like geometry of six sample H II regions (red dots). Visibly, when the shell-like geometry is adopted, the inferred electron densities (linear diameters) are ∼100 times higher (∼10 times smaller) than the values obtained using correspondingly larger volumes. In the absence of these large/small electron densities/linear diameters, the n_e–d distribution is flatter and can be well represented by a power law with spectral index > -1. However, when the effective size of the source is correctly evaluated, the best-fit relation ($n_e \sim d^{-1.45}$) steepens significantly,

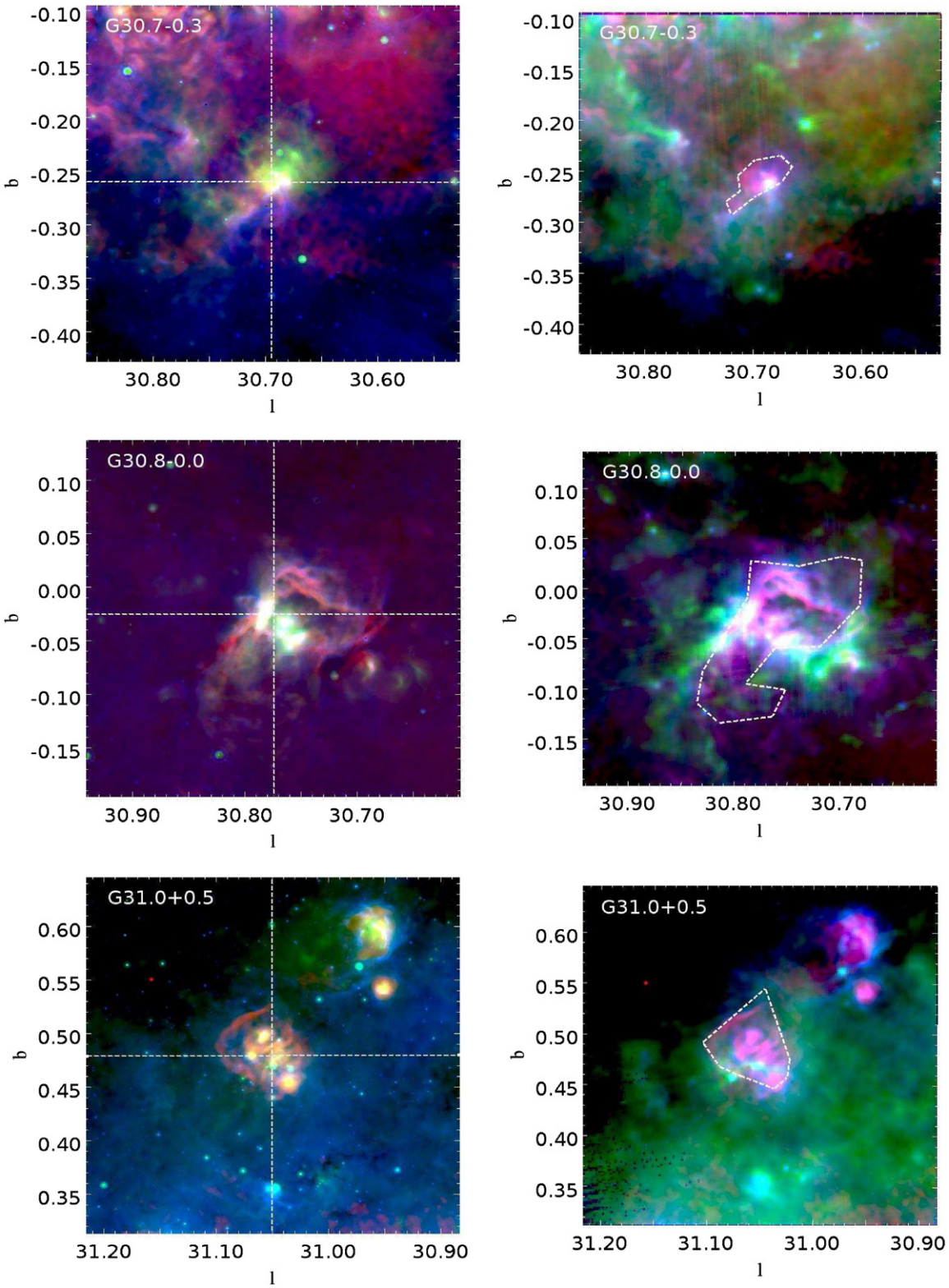

Figure 4. (Continued)

ruling out the possibility that a significant amount of dust is present in the sample H II regions.

7. IR EXCESS

The presence of dust inside H II regions can also be investigated in terms of energy budget, through the so-called *Infrared Excess* (Garay et al. 1993):

$$\mathrm{IRE} = \frac{L_{\mathrm{IR}}}{L(\mathrm{Ly}\alpha)}, \tag{13}$$

where L_{IR} is the IR luminosity and $L(\mathrm{Ly}\alpha)$ is the Lyman photon luminosity derived in Section 3. Evaluation of the IRE provides an estimate of the fraction of photons emitted by the

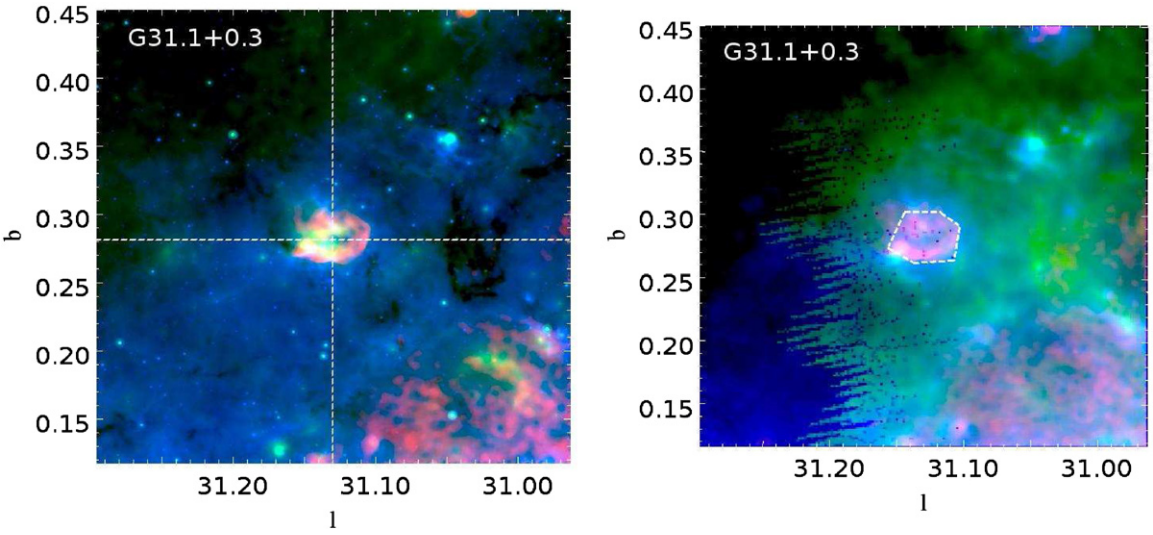

Figure 4. (Continued)

Table 6
Luminosities and IR Excess

Name	$\log(N_{\rm Lyc})$ (s^{-1})	$\log(L({\rm Ly}\,\alpha)/L_\odot)$	$\log(L_{\rm IR,H\,II}/L_\odot)$	$\log(L_{\rm IR,PDR+H\,II}/L_\odot)$	$\rm IRE_{H\,II}$	$\rm IRE_{PDR+H\,II}$
G28.8−0.2	48.67	4.32	4.37	5.22	1.01	1.21
G29.0−0.6	48.07	3.7	4.5	4.95	1.21	1.34
G29.1−0.0	49.39	5.05	5.22	5.74	1.03	1.14
G29.1+0.4	49.69	5.34	5.55	6.14	1.04	1.15
G29.2−0.0	49.43	5.08	5.64	5.97	1.11	1.17
G30.1−0.2	48.86	4.51	4.71	5.13	1.04	1.14
G30.2−0.1	48.95/49.20	4.60/4.85	3.46/3.71	5.29/5.54	0.75/0.76	1.15/1.14
G30.3−0.0	48.47	4.13	4.52	4.92	1.09	1.19
G30.4−0.2	49.38	5.04	5.96	6.29	1.18	1.25
G30.5−0.3	49.22	4.88	5.21	5.66	1.07	1.16
G30.5+0.4	48.46/49.43	4.11/5.08	4.61/5.57	4.73/5.69	1.21/1.10	1.15/1.12
G30.6−0.1	49.10	4.75	5.09	5.36	1.07	1.13
G30.7−0.3	49.35	5.00	5.55	5.96	1.11	1.19
G30.8−0.0	50.29	5.95	6.62	6.89	1.11	1.16
G31.0+0.5	49.46	5.11	5.86	6.01	1.15	1.17
G31.1+0.3	48.79	4.45	4.80	5.23	1.08	1.17

Notes. Lyman-continuum flux ($N_{\rm Lyc}$), Lyα luminosity (L(Lyα)), IR luminosity ($L_{\rm IR,H\,II}$ and $L_{\rm IR,PDR+H\,II}$), and IR excess ($\rm IRE_{H\,II}$ and $\rm IRE_{PDR+H\,II}$) for the 16 H II regions (and associated PDRs) in our sample.

central source and directly absorbed by dust particles. We computed the IRE both for H II regions only and for the combined H II regions and associated PDRs. For H II regions, the IR luminosity was obtained by integration of the best-fit two-temperature component models ($\widetilde{S_{\lambda,2}}$) derived in Section 4.2:

$$L_{\rm IR,H\,II} = 4\pi\, D^2 \int_{\lambda_{\rm min}}^{\lambda_{\rm max}} \widetilde{S_{\lambda,2}}\, d\lambda. \qquad (14)$$

In the expression above, we set $\lambda_{\rm min} = 1\,\mu$m and $\lambda_{\rm max} = 10^4\,\mu$m, and D^2 is, for each source, the heliocentric distances provided in Table 1. In order to estimate the IR luminosities for the (H II region + PDR) ensembles, we performed photometric measurements between 24 μm and 500 μm by including in the aperture not only the region identified by the MAGPIS 20 cm contours, but also the PDR. For this purpose, instead of using the MAGPIS 20 cm data to generate our apertures, we used the IRAC 8 μm images. Following the same steps described in Section 4, we estimated and removed the free–free contribution in each band, and fitted the resulting SEDs with a two-temperature component model with $\beta_{\rm dust} = 2$. $L_{\rm IR,H\,II+PDR}$ for each source was then evaluated by applying a relation similar to Equation (14). The derived $L_{\rm IR,H\,II}$, $L_{\rm IR,H\,II+PDR}$, $\rm IRE_{H\,II}$, and $\rm IRE_{H\,II+PDR}$ are shown in Table 6. For all the sources (with one exception, i.e., G30.2−0.1), both $\rm IRE_{H\,II}$ and $\rm IRE_{H\,II+PDR}$ are slightly (but consistently) greater than 1. Although consistent within the error bars, $\rm IRE_{H\,II+PDR}$ has a tendency to be higher than $\rm IRE_{H\,II}$, and $\overline{IRE_{\rm H\,II}} = 1.08 \pm 0.14$ and $\overline{IRE_{\rm H\,II+PDR}} = 1.17 \pm 0.04$. As expected, this result indicates that the amount of radiation absorbed in the PDR is larger than the amount absorbed in situ. It also shows that, if dust co-exists with the ionized gas in the interior of H II regions, its mass is not significant, in agreement with what we found from the analysis of the n_e–d relation described in the previous section. Finally, we note that the values of IRE obtained for the present sample of H II regions are substantially lower (a factor of 10 on average) than the IR excess reported by Garay et al. (1993). This is likely a consequence of the different evolutionary stage of the

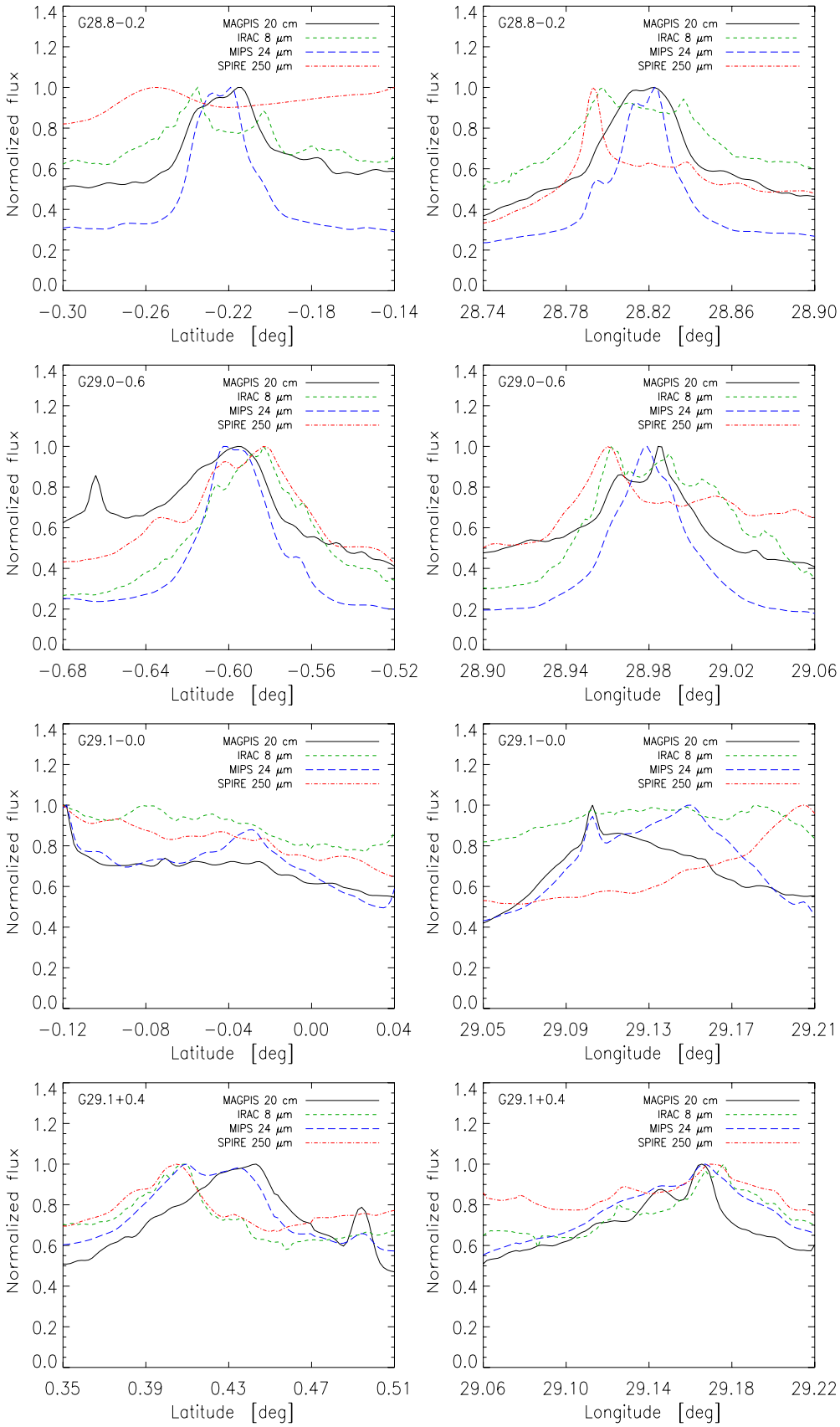

Figure 5. Longitude (right) and latitude (left) profiles, obtained by *slicing* MAGPIS 20 cm, IRAC 8 μm, MIPS 24 μm, and SPIRE 250 μm postage-stamp images of the sources. All images are convolved to SPIRE 250 μm resolution (18″) prior to *slicing*.

(A color version of this figure is available in the online journal.)

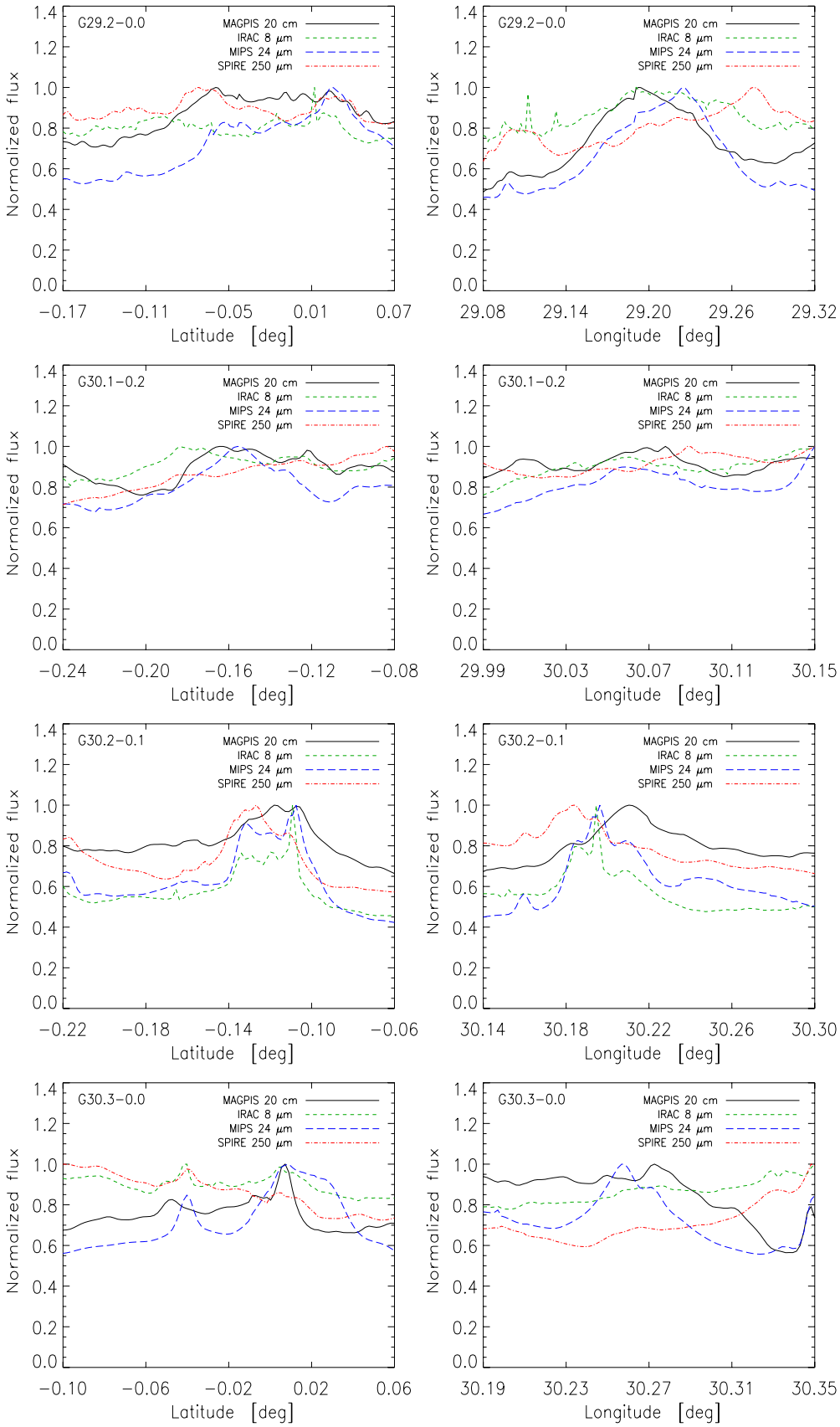

Figure 5. (Continued)

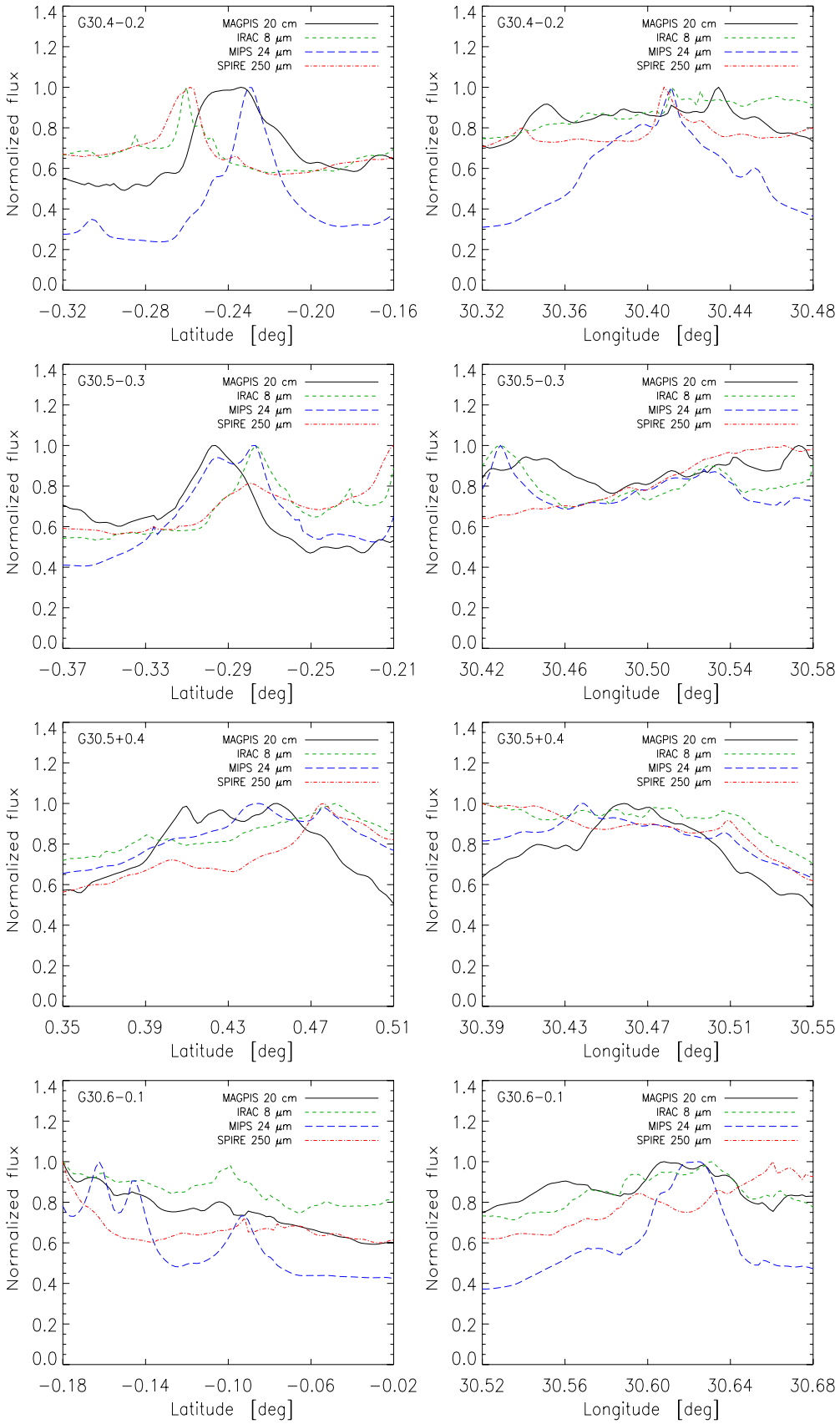

Figure 5. (Continued)

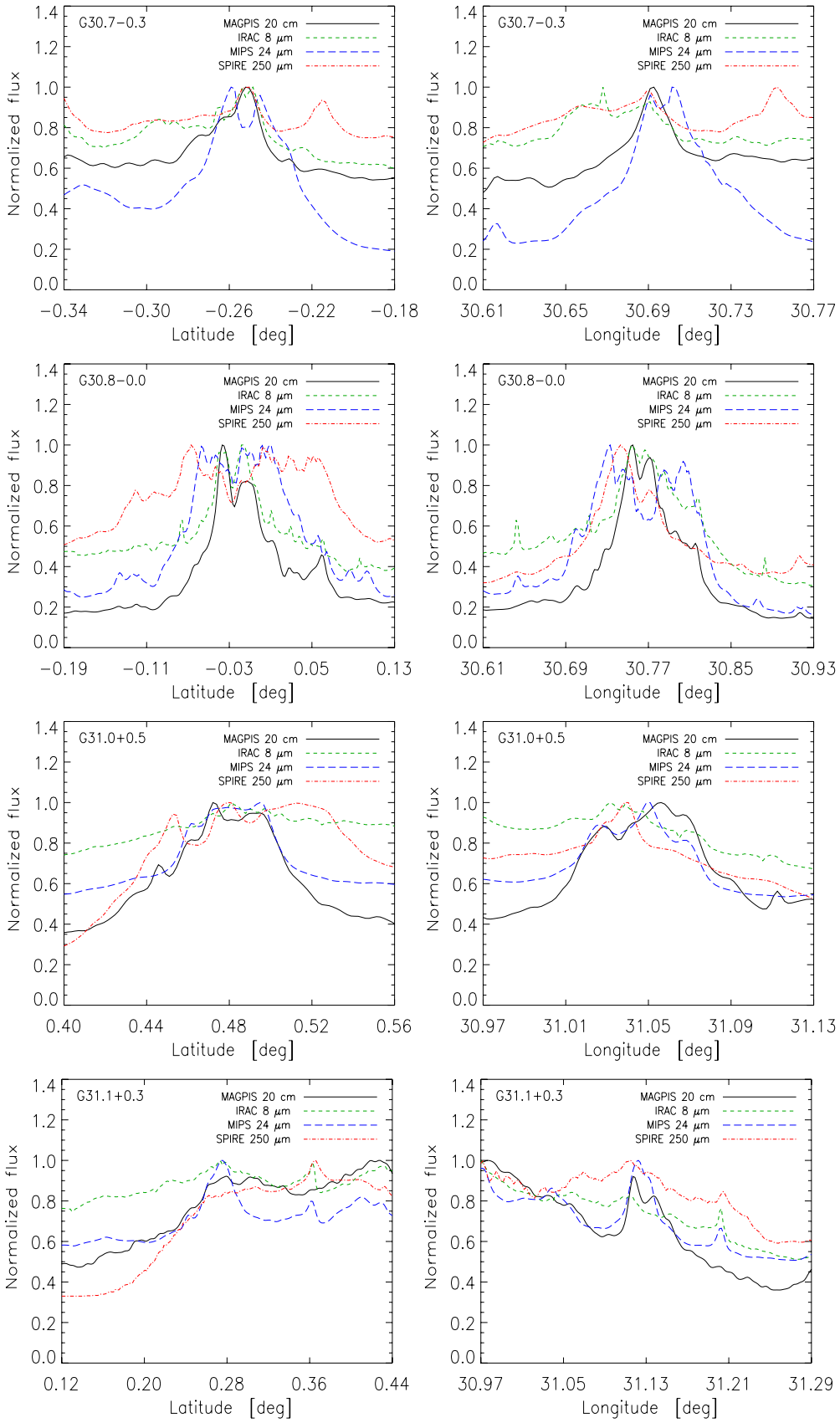

Figure 5. (Continued)

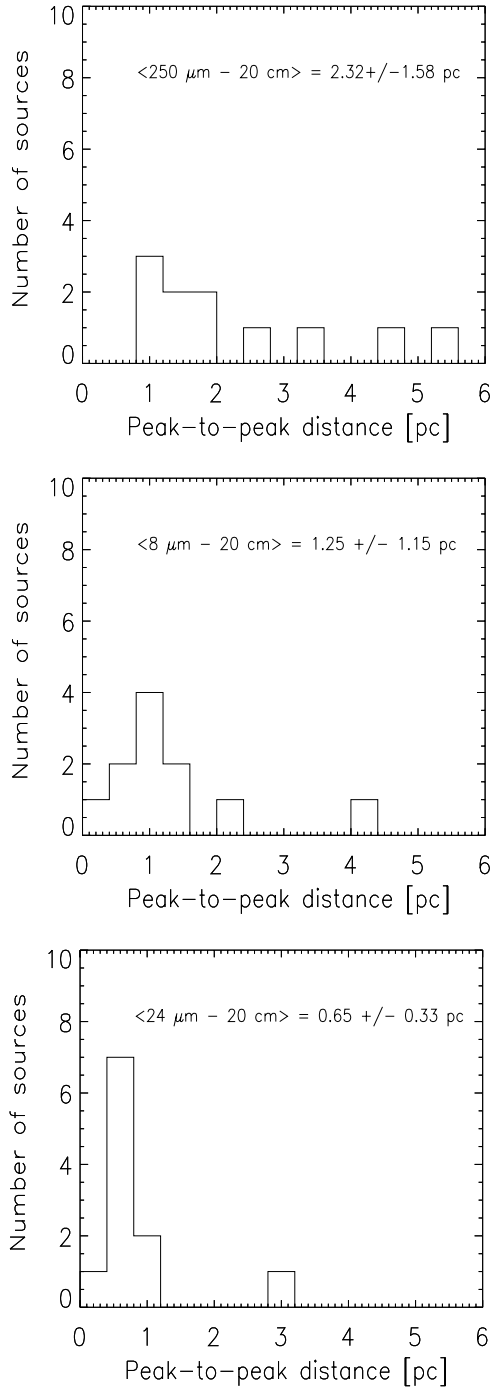

Figure 6. Top to bottom panel: distributions of the linear separation between the peaks of emission of, respectively, SPIRE 250 μm, IRAC 8 μm, and MIPS 24 μm with respect to MAGPIS 20 cm.

sources in the two samples: the sources we are considering are more evolved and less dusty, while the compact H II regions analyzed by Garay et al. (1993) are still embedded in the natal cocoon.

The photometric measurements for both the H II regions and the (H II region + PDR) systems allowed us, as well as to derive IR luminosities, to carry out a qualitative comparison between the average behavior of their SEDs in the wavelength range 24 μm $< \lambda <$ 500 μm. The average SEDs, for the H II regions and (H II region + PDR) systems separately, were obtained by first normalizing each individual SED to its peak and then by taking the average of these normalized SEDs. The result is

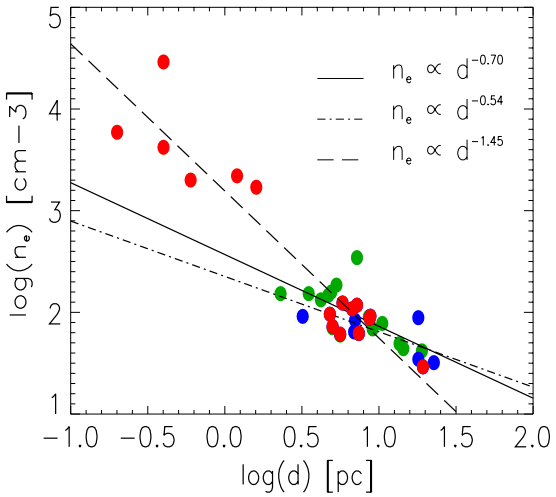

Figure 7. Electron density–size relation derived from: (1) single-dish 6 cm data (green circles, solid line), (2) MAGPIS 20 cm data (blue circles, dashed-dotted line), and (3) MAGPIS 20 cm data (red circles, dashed line), taking into account the potential shell-type morphology of six sample H II regions.

(A color version of this figure is available in the online journal.)

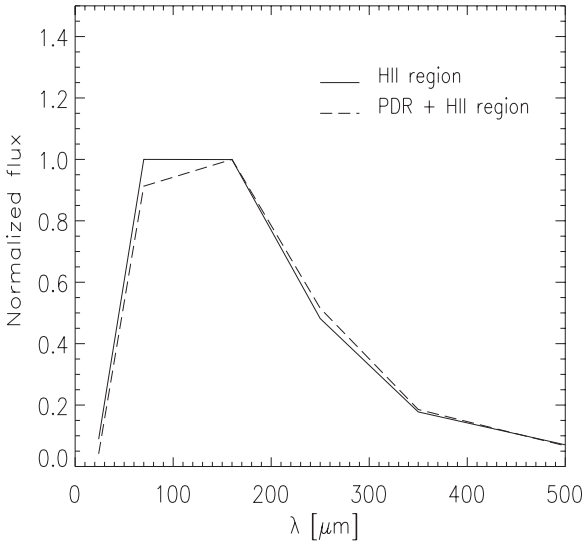

Figure 8. Average H II region (solid line) and PDR (dashed line) SED. The average is taken over the sample of 16 sources considered for this analysis.

illustrated in Figure 8. The peak of the H II regions SED is shifted toward shorter wavelengths (∼70 μm) with respect to the (H II regions + PDRs) SED peak (∼160 μm). This trend is in agreement with the finding of Povich et al. (2007) and can be ascribed to the higher temperature of the dust grain population in the H II region compared to the temperature of the grain population located in the PDR.

8. COLOR–COLOR PLOTS

We used the fluxes extracted in the previous section for the (H II region + PDR) complexes to generate color–magnitude and color–color plots. The goal of this exercise was to look for characteristic colors that can allow the identification of this class of objects with respect to other populations of Galactic sources. In particular, we considered sources in either an earlier or a later evolutionary stage with respect to our sample H II regions. Approximately 100 sources listed in the Hi-GAL preliminary

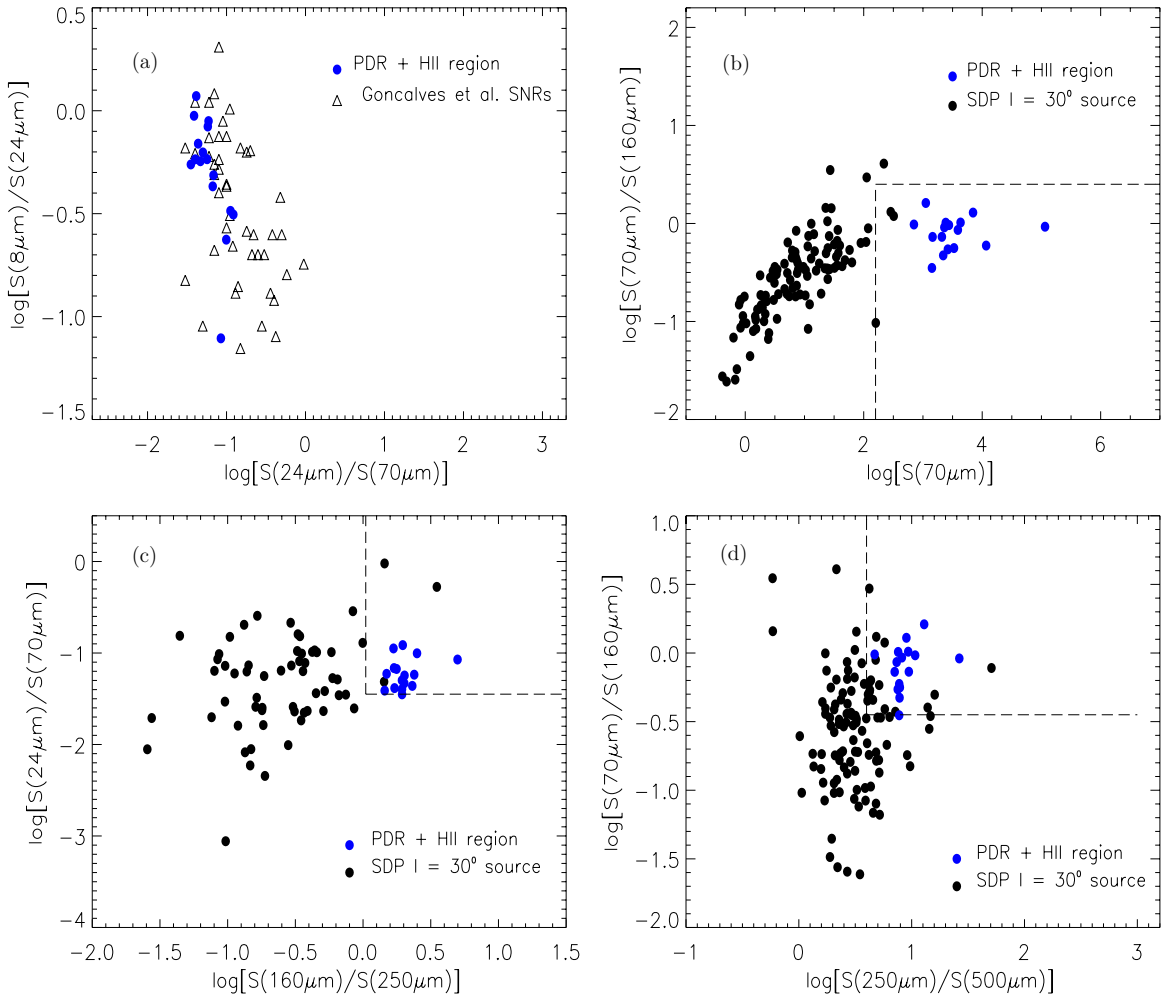

Figure 9. Color–color diagrams obtained by combining PACS (70 μm and 160 μm) and SPIRE (250 μm, 350 μm, and 500 μm) wavelengths, as well as IRAC 8 μm and MIPS 24 μm. Shown in the plots are the 16 evolved H II regions + PDRs of this work (blue filled circles), the Hi-GAL point sources from Elia et al. (2010, black filled circles), and the SNRs from Pinheiro Gonçalves et al. (2011), (black triangles).

(A color version of this figure is available in the online journal.)

catalog (Elia et al. 2010) and located in our $2^\circ \times 2^\circ$ SDP field fall into the former category (e.g., younger sources). These sources have measured fluxes at all PACS and SPIRE wavelengths and at 24 μm. Most of them are thought to be young stellar objects (YSOs; Elia et al. 2010). For the latter category (e.g., older sources), we made use of the 39 supernova remnants (SNRs) cataloged by Pinheiro Gonçalves et al. (2011, hereafter PG11), based on GLIMPSE and MIPSGAL data.

The color–magnitude and color–color diagrams are shown in Figure 9. Panels (b), (c), and (d) highlight the general segregation of the (H II regions + PDRs) with respect to the YSO population. This effect can be attributed to the relatively high dust temperatures ($\sim$30–50 K) characterizing the (H II region + PDR) systems, which causes the peak of their SED to occur at wavelengths shorter than $\simeq$160 μm (see Figure 8 and Section 7). Conversely, in the very early stages of star formation (e.g., YSOs) typical dust temperatures do not go beyond $\sim$15 K, with the consequence that the SED peak is located at $\lambda > 160$ μm. In practice, while the SED of an (H II region + PDR) is rising fast between 24 μm and 70 μm and dropping rapidly between 160 μm and 250 μm (and between 250 μm and 500 μm), that of a YSO is also rising in the 24 μm $< \lambda <$ 70 μm but much more slowly, while for 160 μm $< \lambda <$ 250 μm (and 250 μm $< \lambda <$ 500) it keeps steepening or, if it drops, it drops slowly. Since the Hi-GAL preliminary catalog was not band-merged with the GLIMPSE 8 μm catalog, we were not able to compare the mid-IR color distribution of the (H II region + PDR) population with that of YSOs.

Panel (a) illustrates the behavior of the (H II region + PDR) systems compared to that of SNRs in the 8 μm/24 μm versus 24 μm/70 μm color–color space. Both populations appear to span quite a wide range of 8 μm/24 μm ratios. However, while SNRs also stretch along the *X*-axis direction for an order of magnitude, the H II regions + PDRs are confined to a narrow range of 24 μm $< \lambda <$ 70 μm values. The relatively spread out distribution of SNRs likely reflects the variety of morphologies and emission mechanisms highlighted in PG11. It is worth mentioning that a partial overlap of mid-IR colors for the composite (H II region + PDR) systems and SNRs was already reported by Arendt (1989). A search for Hi-GAL counterparts of the SNRs in the PG11 catalog is currently ongoing (A. Noriega-Crespo et al., in preparation). Preliminary results suggest that the detection rate in the PACS 70 μm band should match the MIPSGAL one, while only few, very bright SNRs (e.g., G11) are detected at 160 μm, and almost none in the SPIRE bands. This effect is currently interpreted as either due to an intrinsic

lack of emission from these sources at far-IR wavelengths or to a competing background level.

9. CONCLUSIONS

The analysis of *Spitzer* IRAC and MIPS data combined with *Herschel* PACS and SPIRE data for a uniform sample of evolved H II regions shows that the emission in the direction of these sources in the range 24 μm–500 μm is well represented (for all but three sources) by a two-temperature dust component model with $\beta_{\rm dust} = 2$. Of these two components, the cold one is in the range 20–30 K and the warm one is in the range 50–90 K. For one of the sources, G30.1−0.2, a one-temperature component model with a varying spectral emissivity index appears to be a better representation of the observed SED, although in this case the $\beta_{\rm dust}$ (0.32) retrieved from the fit is outside the range of commonly accepted values. For two other sources, G30.3−0.0 and G30.6−0.1, neither a modified blackbody with $\beta_{\rm dust}$ kept as a free parameter nor a two-temperature component model with fixed $\beta_{\rm dust}$ agrees with the measurements in a satisfactory fashion. We emphasize that, for all the sample sources, the temperatures obtained for the warm component are not well constrained due to a lack of measurements between 24 μm and 70 μm. Despite this limitation, these results highlight the importance of including bands shorter than 100 μm for studying sources, such as H II regions, which are characterized by multiple temperature components. In fact, when the shorter wavelengths are not considered in the fitting process, the cold component, as well as the warm one, might not be correctly constrained.

Our study strongly suggests that dust is present in the interior of H II regions. Three complementary pieces of evidence are found in support of this conclusion:

1. a statistically significant flux detection, after background subtraction, for 8 μm $< \lambda <$ 500 μm (with an average S/N greater than or of the order of three);
2. a slope for the n_e–d relation slightly steeper than −1.5; and
3. values of IRE > 1 for the entire sample H II regions.

It is noteworthy that although the data seemed to favor the existence of dust grains in the interior of evolved H II regions, the amount of dust in these environments is likely not significant. We also remind the reader that, based on our analysis, we cannot completely rule out the possibility that the detected IR emission is due to background/foreground radiation along the line of sight.

We argue that partial dust depletion within H II regions appears to be caused primarily by radiation-pressure drift, as recently proposed by Draine (2011). In this light, we speculate that the observed 24 μm emission cannot be attributed to a dust population (either VSGs or BGs) coeval with respect to the BGs and PAHs located in the surrounding PDR, but rather to a new generation of grains, in agreement with what was recently suggested by Everett & Churchwell (2010) for the case of WBB.

Finally, we show that far-IR colors can be reliably used for identifying unresolved Galactic or extragalactic H II regions with respect to younger populations of sources, such as YSOs. On the contrary, distinguishing unresolved H II regions from SNRs based solely on mid-IR colors appears to be more challenging, and may require the additional use of ancillary data, such as radio continuum or RRLs.

The authors thank the anonymous referee for comments which allowed us to greatly improve the content and presentation of the paper.

REFERENCES

Agladze, N. I., Sievers, A. J., Jones, S. A., et al. 1996, ApJ, 462, 1026
Aguirre, J. E., Ginsburg, A. G., & Dunham, M. K. 2011, ApJS, 192, 4
Altenhoff, W. J., Downes, D., Pauls, T., et al. 1979, A&AS, 35, 23
Anderson, L. D., & Bania, T. M. 2009, ApJ, 690, 706
Anderson, P. W., Halperin, B. I., & Varma, C. M. 1972, Philos. Mag., 25, 1
Anderson, L. D., Zavagno, A., Rodon, J. A., et al. 2010, A&A, 518, 99
Arendt, R. G. 1989, ApJS, 70, 181
Arthur, S. J., Henney, W. J., Mellema, G., et al. 2011, MNRAS, 414, 1747
Bally, J., Anderson, L. D., Battersby, C., et al. 2010, A&A, 518, 90
Beckert, T., Duschl, W. J., & Mezger, P. G. 2000, A&A, 356, 1149
Benjamin, R. A., Churchwell, E., Babler, B. L., et al. 2003, PASP, 115, 953
Bennett, C. L., Smoot, G. F., Hinshaw, G., et al. 1992, ApJ, 396, 7
Bernard, J.-P., Paradis, D., Marshall, D. J., et al. 2010, A&A, 518, 88
Boudet, N., Mutschke, H., Nayral, C., et al. 2005, ApJ, 633, 272
Boulanger, F., & Perault, M. 1988, ApJ, 330, 964
Carey, S. J., Noriega-Crespo, A., Mizuno, D. R., et al. 2009, PASP, 121, 76
Chini, R., Kreysa, E., Kruegel, E., & Mezger, P. G. 1986a, A&A, 166, 8
Chini, R., Kreysa, E., Mezger, P. G., et al. 1986b, A&A, 154, 8
Chini, R., Kreysa, E., Mezger, P. G., et al. 1986c, A&A, 157, 1
Chini, R., Kruegel, E., & Wargau, W. 1987, A&A, 181, 378
Churchwell, E., Povich, M. S., Allen, D., et al. 2006, ApJ, 649, 759
Comeron, F. 1997, A&A, 326, 1195
Compiegne, M., Abergel, A., Verstrate, L., et al. 2007, A&A, 471, 205
Compiegne, M., Verstraete, L., Jones, A., et al. 2011, A&A, 525, 103
Condon, J. J. 1992, ARA&A, 30, 575
Deharveng, L., Pena, M., Caplan, J., et al. 2000, MNRAS, 311, 329
Deharveng, L., Schuller, F., Anderson, L. D., et al. 2010, A&A, 523, 6
Desert, F.-X., Macias-Perez, J. F., Mayet, F., et al. 2008, A&A, 481, 411
Diolati, E., et al. 2000, A&AS, 147, 335
Downes, D., Wilson, T. L., Bieging, J., & Wink, J. 1980, A&AS, 40, 379
Draine, B. T. 2011, ApJ, 723, 100
Dupac, X., Bernard, J.-P., Boudet, N., et al. 2003, A&A, 404, 11
Elia, D., Schisano, E., Molinari, S., et al. 2010, A&A, 518, 97
Everett, J. E., & Churchwell, E. 2010, ApJ, 713, 592
Flagey, N., Boulanger, F., Noriega-Crespo, A., et al. 2011, A&A, 531, 51
Forbes, D. 1989, A&AS, 77, 439
Gail, H.-P., & Sedlmayr, E. 1979, A&A, 76, 158
Garay, G., & Lizano, S. 1999, PASP, 111, 1049
Garay, G., Rodriguez, L. F., & Moran, J. M. 1993, ApJ, 418, 368
Griffin, M. J., Abergel, A., Abreau, A., et al. 2010, A&A, 518, 3
Helfand, D. J., Becker, R. H., & White, R. L. 2006, AJ, 131, 2525
Hollenbach, D. J., & Tielens, A. G. G. 1997, ARA&A, 35, 179
Inoue, A. K. 2002, ApJ, 570, 688
Kelsall, T., Weiland, J. L., Franz, B. A., et al. 1998, ApJ, 508, 44
Kemper, F., Vriend, W. J., & Tielens, A. G. G. M. 2004, ApJ, 609, 826
Kim, K.-T., & Koo, B.-C. 2001, ApJ, 549, 979
Krumholz, M. R., & Matzner, C. D. 2009, ApJ, 703, 1352
Kuchar, T. A., & Clark, F. O. 1997, ApJ, 488, 224
Kurtz, S. 2005, in Proc. IAU Symp. 227, Massive Star Birth: A Crossroads of Astrophysics, ed. R. Cesaroni, M. Felli, E. B. Churchwell, & C. M. Walmsley (Cambridge: Cambridge Univ. Press), 111
Lagache, G., Haffner, L. M., Reynolds, R. J., & Tufte, S. L. 2000, A&A, 354, 247
Lockman, F. J. 1989, ApJS, 71, 469
Lewis, A., & Bridle, S. 2002, Phys. Rev. D, 66, 10
Masi, S., Aquilini, E., Boscaleri, A., et al. 1995, ApJ, 452, 253
McClure-Griffiths, N. M., & Dickey, J. M. 2007, ApJ, 671, 427
McKee, C. F., & Williams, J. P. 1997, ApJ, 476, 144
Mennella, V., Brucato, J. R., Colangeli, L., et al. 1998, ApJ, 496, 1058
Meny, C., Gromov, V., Boudet, N., et al. 2007, A&A, 468, 171
Mezger, P. G., & Henderson, A. P. 1967, ApJ, 147, 471
Molinari, S., Swinyard, B., Bally, J., et al. 2010, A&A, 518, 100
Mookerjea, B., & Ghosh, S. K. 1999, Bull. Astron. Soc. India, 27, 567
Paladini, R., Burigana, C., & Davies, R. D. 2003, A&A, 397, 213
Paladini, R., Montier, L., Giard, M., et al. 2007, A&A, 465, 839
Paradis, D., Paladini, R., Noriega-Crespo, A., et al. 2011, ApJ, 735, 6
Paradis, D., Veneziani, M., Noriega-Crespo, A., et al. 2010, A&A, 520, 8
Phillips, W. A. 1972, J. Low Temp. Phys., 7, 351
Pilbratt, G. L., Riedinger, J. R., Passvogel, T., et al. 2010, A&A, 518, L1

Pinheiro Gonçalves, D., Noriega-Crespo, A., Paladini, R., Martin, P. G., & Larey, S. J. 2011, AJ, 142, 47
Planck Collaboration 2010, A&A, 536, 21
Poglitsch, A., Waelkens, C., Geis, N., et al. 2010, A&A, 518, 2
Povich, M. S., Stone, J. M., Churchwell, E., et al. 2007, ApJ, 660, 346
Price, S. D., Egan, M. P., Carey, S. J., et al. 2001, AJ, 121, 2819
Quireza, C., Rood, R. T., Bania, T. M., et al. 2007, ApJ, 653, 1226
Rodon, J. A., Zavagno, A., Baluteau, J.-P., et al. 2010, A&A, 518, 80
Rosolowsky, E., Dunham, M. K., Ginsburg, A., et al. 2010, ApJS, 188, 123
Schuller, F., Menten, K. M., Contreras, Y., et al. 2009, A&A, 504, 415
Shetty, R., Kauffmannm, J., Schnee, S., et al. 2009, ApJ, 696, 2234
Simon, R., Jackson, J. M., & Clemens, D. P. 2001, ApJ, 551, 747
Smith, L. F., Biermann, P., & Mezger, P. G. 1978, A&A, 66, 65
Traficante, A., Calzoletti, L., Veneziani, M., et al. 2011, MNRAS, 416, 2932
Veneziani, M., Ade, P. A. R., Bock, J. J., et al. 2010, ApJ, 702, 61
Watson, C., Povich, M. S., Churchwell, E. B., et al. 2008, ApJ, 681, 1341
Werner, M., Roelling, T., Low, F., et al. 2004, ApJS, 154, 1
Zavagno, A., Anderson, L. D., Russeil, D., et al. 2010, A&A, 518, 101